INSTITUTO TECNOLOGICO Y DE ESTUDIOS
SUPERIORES DE MONTERREY
CAMPUS MONTERREY
SCHOOL OF ENGINEERING
DIVISION OF MECHATRONICS AND INFORMATION
TECHNOLOGIES
GRADUATE PROGRAM

DOCTOR OF PHILOSOPHY
in
INFORMATION TECHNOLOGIES AND COMMUNICATIONS
MAJOR IN OPTICS

Implementation of a two-photon Michelson interferometer for
Quantum-Optical Coherence Tomograhy

By
Dorilián López Mago

MAY 2012

INSTITUTO TECNOLOGICO Y DE ESTUDIOS SUPERIORES DE MONTERREY

CAMPUS MONTERREY

SCHOOL OF ENGINEERING

DIVISION OF MECHATRONICS AND INFORMATION TECHNOLOGIES

GRADUATE PROGRAM

DOCTOR OF PHILOSOPHY

in

INFORMATION TECHNOLOGIES AND COMMUNICATIONS

MAJOR IN OPTICS

Implementation of a two-photon Michelson interferometer for
Quantum-Optical Coherence Tomograhy

By

Dorilián López Mago

MAY 2012

INSTITUTO TECNOLÓGICO Y DE ESTUDIOS SUPERIORES DE MONTERREY
CAMPUS MONTERREY

SCHOOL OF ENGINEERING
DIVISION OF MECHATRONICS AND INFORMATION
TECHNOLOGIES
GRADUATE PROGRAM

DOCTOR OF PHILOSOPHY
in
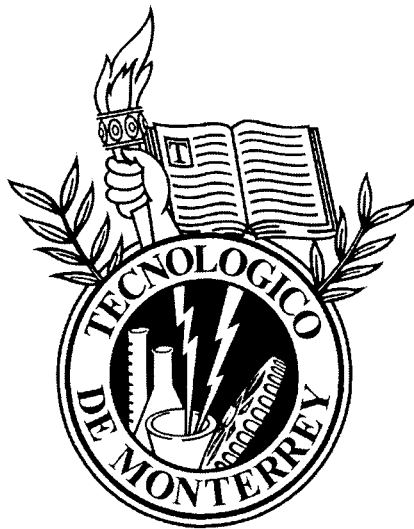INFORMATION TECHNOLOGIES AND COMMUNICATIONS
MAJOR IN OPTICS

**Implementation of a two-photon Michelson interferometer for
Quantum-Optical Coherence Tomography**

By

Dorilián López Mago

MAY 2012

Implementation of a two-photon Michelson interferometer for Quantum-Optical Coherence Tomography

A dissertation presented by

Dorilián López Mago

Submitted to the
Graduate Programs in Mechatronics and Information Technologies
in partial fulfillment of the requirements for the degree of

Doctor of Philosophy
in
Information Technologies and Communications
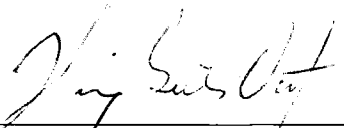Major in Optics

Thesis Committee:

Dr. Julio C. Gutiérrez Vega	-	Tecnológico de Monterrey
Dr. Lukas Novotny	-	The University of Rochester
Dr. Raúl I. Hernández Aranda	-	Tecnológico de Monterrey
Dr. Servando López Aguayo	-	Tecnológico de Monterrey
Dr. Carlos López Mariscal	-	Naval Research Laboratory
Dr. Rodolfo Rodríguez y Masegosa	-	Tecnológico de Monterrey

Instituto Tecnológico y de Estudios Superiores de Monterrey
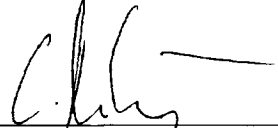Campus Monterrey
May 2012

Instituto Tecnológico y de Estudios Superiores de Monterrey
Campus Monterrey

Division of Mechatronics and Information Technologies
Graduate Program

The committee members, hereby, certify that have read the dissertation presented by Dorilián López Mago and that it is fully adequate in scope and quality as a partial requirement for the degree of **Doctor of Philosophy in Information Technologies and Communications**, with a major in **Optics**.

Dr. Julio C. Gutiérrez Vega
Tecnológico de Monterrey
Principal Advisor

Dr. Lukas Novotny
The University of Rochester
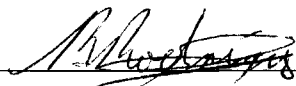Committee Member

Dr. Raúl I. Hernández Aranda
Tecnológico de Monterrey
Committee Member
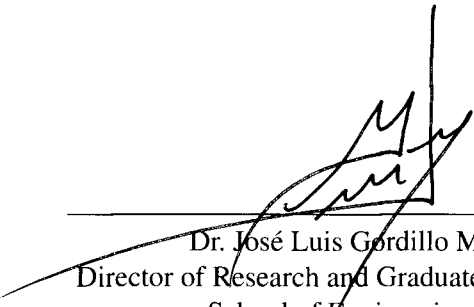
Dr. Servando López Aguayo
Tecnológico de Monterrey
Committee Member

Dr. Carlos López Mariscal
Naval Research Laboratory
Committee Member

Dr. Rodolfo Rodríguez y Masegosa
Tecnológico de Monterrey
Committee Member

Dr. José Luis Gordillo M.
Director of Research and Graduate Programs
School of Engineering

Copyright Declaration

I, hereby, declare that I wrote this dissertation entirely by myself and, that, it exclusively describes my own research.

Dorilián López Mago
Monterrey, N.L., México
May 2012

A mis padres,
por su interminable apoyo.

Acknowledgements

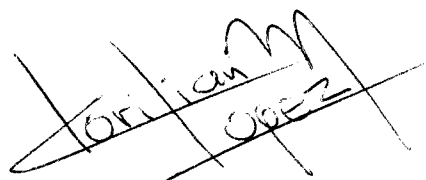First of all, I would like to express my gratitude to Prof. Julio C. Gutiérrez Vega, my thesis advisor, for his support, guidance and example. My desires for pursuing a research career were highly influenced by his teachings. I appreciate the opportunity to pursue my own research interests. To the members of my thesis committee, Rodolfo Rodríguez y Masegosa, Raul I. Hernández Aranda, Servando López Aguayo, Carlos López Mariscal and Lukas Novotny. Thanks for taking the time to read my thesis, for the comments and feedback.

I thank Lukas Novotny for letting me being part of his group and for encouraging me to do experimental work. Thanks to the nano-optics group for their suggestions and help in the development of my experiment and for the good coffee.

To my friends and coworkers from La Pecera: Polo, Raul, Ruelas, Servando, Sosa, Manuel and Antonio for helpful and lively discussions. Thanks to the energy group, Fran, George, Robert and Romo for bringing the challenge to the basketball games and to the rest of the physics department for their support.

I am grateful to the Monterrey SPIE chapter for their help and support in the development of outreach projects. Particularly to Adad, Robin, Juan Carlos and Thalia for their ideas, motivation and support. The successful of the chapter would not have been possible without them.

Thanks to my friends Adad, Robin, Polo, Margarita, Juan Carlos and Ruelas for their company, conversations and hours of fun. Particularly to my best friend Juan Carlos that, even with all our differences and deadly discussions, we have been friends since he was known as Rojas.

Great thanks to my family. To my parents and my sister for their never-ending support and understanding. To my brother for his charisma and energy. To Sashaira for her constant support. Thanks to the rest of my family for considering me as example.

Finally, I acknowledge CONACYT for the financial support. I believe that Mexico has potential for becoming an important player in the scientific development and appreciate the effort of CONACYT for pursuing that goal.

In science, it is when we take some interest in the great discoverers and their lives that it becomes endurable, and only when we begin to trace the development of ideas that it becomes fascinating.

James Clerk Maxwell

Implementation of a two-photon Michelson interferometer for Quantum-Optical Coherence Tomography

by

Dorilián López Mago

Abstract

Time-domain Optical Coherence Tomography (OCT) is an imaging technique that provides information about the internal structure of a sample. It makes use of classical light in conjunction with conventional interferometers. A quantum version of OCT, called Quantum-Optical Coherence Tomography (QOCT), has been developed in previous years. QOCT uses entangled photon pairs in conjunction with two-photon interferometers. QOCT improves depth resolution and offers more information about the optical properties of the sample. However, the current implementation of QOCT is not competitive with its classical counterpart because of the low efficiency of the current sources and detectors that are required for its implementation.

We analyzed the feasibility of QOCT using a Michelson interferometer that can be adapted to the state of the art in entangled photon sources and detectors. Despite of its simplicity, no current implementations of QOCT have been done with this interferometer. This thesis develops the theory of the two-photon Michelson interferometer applied in QOCT. It describes the elements that characterizes the coincidences interferogram and support the theory with experimental measurements.

We found that as long as the spectral bandwidth of the entangled photons is smaller than their central frequency, the Michelson interferometer can be successfully used for QOCT. In addition, we found that the degree of entanglement between the photons can be calculated from the coincidences interferogram. The two-photon Michelson interferometer provides another possibility for QOCT with the advantages of simplicity, performance and adaptability. The resolution of the interferometer can be improved using ultrabroadband sources of entangled photons, e.g. photonic fibers. In addition, we can study the implementation of photon-number resolving detectors in order to remove the detection of coincidences that is used for detecting entangled photon pairs.

List of Figures

Contents

Chapter 1

Introduction

1.1 Motivation

Optical imaging techniques such as optical coherence tomography (OCT) and confocal microscopy have found widespread applications in medicine. Compared to other imaging techniques, e.g. magnetic resonance imaging, ultrasound and positron emission tomography, they offer micrometer resolution, noninvasive imaging and real time measurements.

The resolution of these optical systems is limited by the wave nature of light. The smallest feature that can be distinguished has a direct Fourier connection with the spectral properties of the light source. It is a consequence of the Heisenberg uncertainty principle, which imposes limits on the precision of measurements. The Heisenberg uncertainty gives rise to the diffraction limit in microscopy and the coherence length in OCT. However, the Heisenberg limit can be overcome using nonclassical states of light such as squeezed and entangled states. Nonclassical (quantum) sources of light have been developed over the past years and promise to enhance the performance of the optical imaging systems.

This thesis studies the quantum version of OCT, called Quantum-Optical Coherence Tomography (QOCT), which makes use of entangled photons. However, the current configuration of QOCT is far away to compete with its classical counterpart because of the low efficiency of the entangled-photon sources that can be used. With this in mind, we propose a new scheme for QOCT based on the standard Michelson interferometer. Besides its practical advantages, this configuration is compatible with current high-flux sources of entangled photons and state of the art detectors. We hope that our results motivate real applications of QOCT.

1.2 Problem Statement and Context

Optical coherence tomography is an interferometric imaging technique that provides cross-sectional images of an object [1]. It has the properties of being a non-invasive and non-contact measurement technique which offers high-resolution images within a short acquisition time. OCT started as a method for finding faults in fiber optical cables and network components and has become a robust technology with applications in medicine [2, 3] and material thickness measurements [4, 5].

Time-domain OCT is a form of low-coherence interferometry. It makes use of the coherence properties of classical light to effectively section a reflective sample with a resolution that is determined by the coherence time of the source. The coherence time is inversely proportional to the source spectral bandwidth. Therefore, sources with a broad spectrum (e.g. superluminescent diodes, ultrashort pulsed lasers and photonic crystal fibers) are used to produce high-resolution images.

The standard configuration of time-domain OCT consists of a Michelson interferometer with a scanning mechanism, as shown in Fig. 1.1a. One arm of the interferometer contains the sample to be explored and the other, the reference arm, introduces a time delay τ. The interference of the reflected light from the sample with the light from the reference mirror, produces an interference pattern or interferogram $I(\tau)$ that contains the information of the internal structure of the sample (Fig. 1.1b).

(a) Michelson interferometer   (b) Interferogram
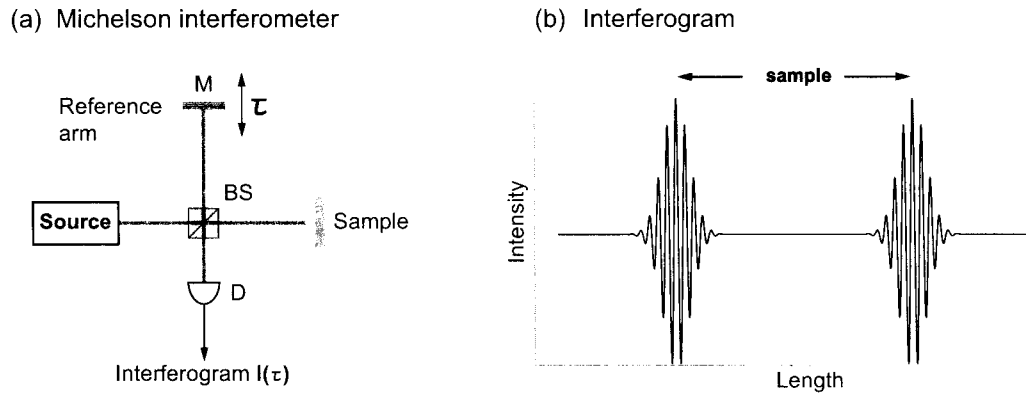
Figure 1.1: Basic principle for Optical Coherence Tomography. (a) A low-coherence light source is used with a Michelson interferometer to record the interference of the reflected light from the sample. The interference pattern or interferogram $I(\tau)$ depends on the time difference τ between the reference arm and the sample arm. (b) Recorded interferogram as a function of the path-length difference between the interferometer arms. The thickness of the sample slab is the distance between the maxima of the interferogram which corresponds to the reflections from the surfaces of the sample. BS: beam splitter, D: detector, M: mirror.

OCT can resolve a minimum distance defined by the source coherence time. Axial resolution is enhanced by increasing the spectral bandwidth of the source. However, as the bandwidth is increased the effects of group-velocity dispersion become apparent. Sample dispersion tends to increase the coherence length and hence to degrade the resolution. In order to counteract the effects of dispersion, a priori knowledge of the dispersion is required.

The development of nonclassical sources of light, such as entangled photons pairs, suggested the idea of using such sources for OCT. Quantum-Optical Coherence Tomography raised as a consequence. QOCT combines the correlation properties of the entangled photons with the capabilities of OCT. It was proposed by Abouraddy et al. [6] in 2002 and experimentally proved by Nasr et al. [7] a year later. Eventually, there have been several improvements in the theory and experimental implementations of QOCT. Furthermore, QOCT has opened

new methods that mimic the quantum properties using classical sources [8].

QOCT uses entangled photon pairs in conjunction with a two-photon interferometer which incorporates two photodetectors working in coincidences, rather than a single photodetector as in OCT. One photon travels to the sample and the other to a controllable delay time. The coincidences of photons arriving at the two detectors are recorded as a function of the delay time. The entanglement between the photons provides high correlations in frequency that cannot be achieved using classical sources. This feature enhances the resolution by a factor of two and makes the interferogram immune to the dispersion effects.

The original version of QOCT uses a Hong-Ou-Mandel (HOM) interferometer [9]. The HOM interferometer consists of a beam splitter where the two photons enter the beam splitter through separate input ports and the coincidences are recorded at the output ports (Fig. 1.2a). The intensity of the coincidences depends on the phase difference between the photons and becomes a minimum at each position of the layers that constitute the sample. The minimum is consequence of the bunching properties of the photons, which means that they tend to exit the beam splitter together through only one of the output ports.
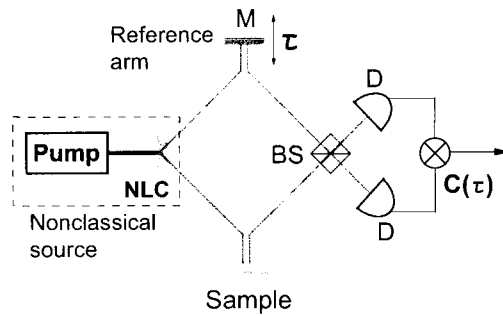
(a) Hong-Ou-Mandel interferometer   (b) Concidence interferogram
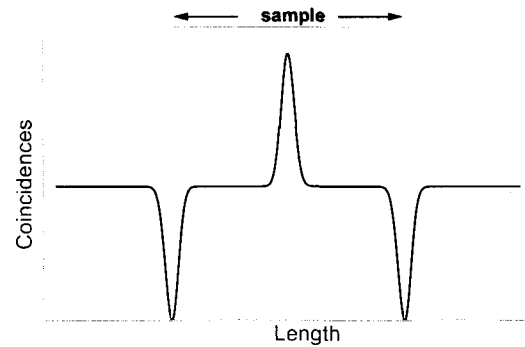
Figure 1.2: Original configuration of Quantum-Optical Coherence Tomography. (a) The Hong-Ou-Mandel interferometer uses a source of entangled photon pairs where both photons meet at a beam splitter through different input ports. At the output of the beam splitter, two detectors measure the coincidences rate $C(\tau)$ as a function of the time delay τ. (b) The coincidences interferogram traces out a dip at each position of the layers. The peak at the middle of the sample is consequence of constructive interference between the reflected light in the second surface and the transmitted light from the first one. BS: beam splitter, D: detector, M: mirror, NLC: nonlinear crystal.

The coincidences interferogram (Fig. 1.2b) contains the location of the internal layers of the sample, which is indicated by the minima. In addition, it provides information about the dispersion properties of medium, which is implicit in the central peak. This peak can be subtracted from the interferogram by averaging over the central frequency of the entangled photons. From the width of this peak, we can obtain the value of the group velocity. This information is not available in OCT.

The source of entangled photons is implemented using the process of Spontaneous Parametric Down-Conversion (SPDC). SPDC originates inside a birefringent crystal with a nonlinear susceptibility. A pump photon propagating inside the nonlinear crystal is spontaneously split into two photons. The direction of the down-converted photons can be controlled by adjusting the angle between the pump photons and the optics axis of the crystal.

The HOM interferometer requires that the entangled photons be emitted noncollinearly (both photons propagate with different directions). This represents a challenge for alignment and balancing of the optical paths. The noncollinear configuration constraints the physical dimensions of the crystals and therefore it is customary to use nonlinear crystals with small dimensions.

The intensity of SPDC is proportional to the interaction volume of the pump with the crystal. As a consequence of the noncollinear configuration, we are restricted to use crystals with small interaction volumes and hence low intensity in the production of entangled photons. The low intensity increases the acquisition time for the recording of the coincidences interferogram. As a comparison, the recording time of a single point in QOCT it is in the order of seconds while for OCT is in milliseconds.

High intensity sources of entangled photons, such as periodically poled crystals [10] and photonic crystal fibers [11], produce collinearly propagating entangled photons. Therefore, the noncollinear configuration of the HOM interferometer is not compatible with this kind of sources.

In principle, the implementation of coincidence detection for measuring nonclassical states is a practical issue rather than a requirement. Instead, it is possible to use photon number detectors [12] which are able to resolve the number of incident photons. The technology is still in development but it promises to eradicate the use of coincidence electronics. Again, the noncollinear configuration of the HOM interferometer is not suitable for this kind of detectors.

In summary, the problem with QOCT is its noncollinear configuration which imposes several challenges and limitations. It is difficult to align and to couple with other optical components, limits the possible sources of entangled photons and its integration with novel detectors.

1.3   Solution Overview

We propose a new implementation of QOCT using a standard Michelson interferometer. The Michelson configuration is attractive because of its simplicity, robustness and integrability. Since the classical OCT uses a Michelson interferometer, it might be apparent that this configuration should be already used for QOCT, but currently neither implementations nor proposals have yet been reported.

It turns out that using the Michelson interferometer, the coincidence interferogram contains more subtleties than the HOM interferogram. However, we found that by Fourier processing the data we can extract the same information that can be achieved with the HOM interferometer.

The configuration is shown in Fig. 1.3a. It uses a *collinear* source of entangled photons which are generated with the process of SPDC. The detection of the photon pairs is obtained using a coincidence detector. The recorded interferogram of a single reflective layer is shown

(a) Two-Photon Michelson interferometer   (b) Coincidences interferogram
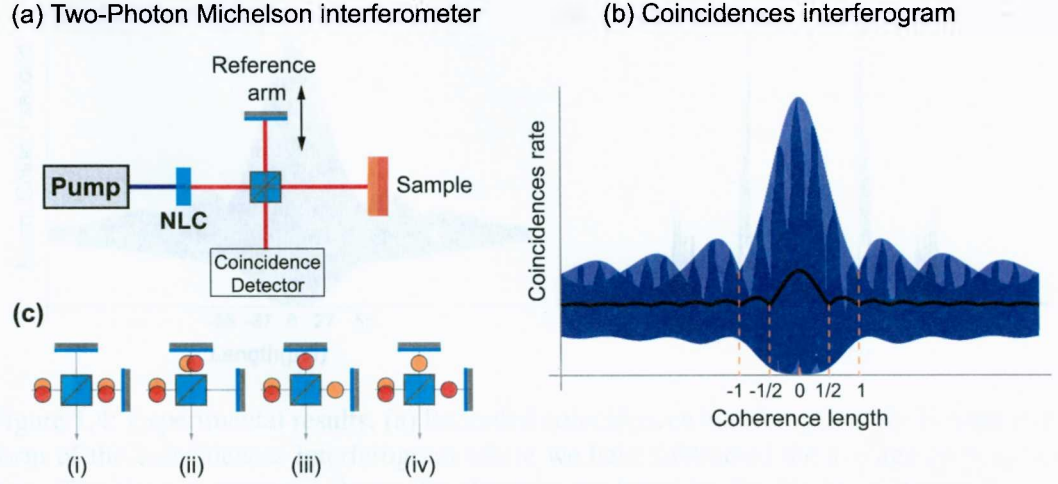
Figure 1.3: (a) Configuration of QOCT using a two-photon Michelson interferometer. It uses collinear entangled photons generated with a nonlinear crystal pumped by a blue laser (407 nm). The entangled photons enter the Michelson interferometer and the coincidences are monitored as a function of the delay τ introduced by the reference arm. (b) Coincidences interferogram for a single reflective layer. The interferogram was calculated using Eq. (1.1). The black solid line is the second term in Eq. (1.1) which provides resolution enhancement by a factor of two. (c) The coincidences interferogram is produced by the superposition of the four possibilities in which the pair of photons can travel through the interferometer. Cases (iii) and (iv) produce the central region of the interferogram whereas cases (i) and (ii) are responsible for the doubling of the frequency of the fringes.

in Fig. 1.3b. We found that the general expression of the coincidences interferogram $C(\tau)$ is given by four contributions

$$C(\tau) \propto M_0 + 2\text{Re}[M_1(2\tau)] + 2\text{Re}[M_2(\tau)e^{-i\omega_0\tau}] + 2\text{Re}[M_3 e^{-i2\omega_0\tau}], \qquad (1.1)$$

where τ is the controllable delay time introduced by the reference arm. To understand the origin of the four terms refer to Fig. 1.3c. When the two photons arrive at the input port of the beam splitter, there are four possibilities for the output: both photons are transmitted (*i*), both are reflected (*ii*), one is transmitted/reflected and the other is reflected/transmitted (*iii* and *iv*). The superposition of these possibilities gives rise to the interference pattern in Eq. (1.1). M_0 is the average number of coincidences. The second and third term are produced by the cases *iii* and *iv*. M_1 and M_2 are envelope functions equivalent to the Fourier transform of the spectral density of the down-converted photons. The cases *i* and *ii* produce the last term of the interferogram.

We found that the second term in Eq. (1.1) is equivalent to the interferogram produced by the HOM interferometer. Notice that the envelope $M_1(2\tau)$ has a smaller coherence length compared to $M_2(\tau)$. In fact, M_1 provides an enhancement in resolution by a factor of two. In addition, the second term is spectrally separated from the other contributions and hence we can Fourier process the interferogram to filter out that term. Fig. 1.4 shows our experimental
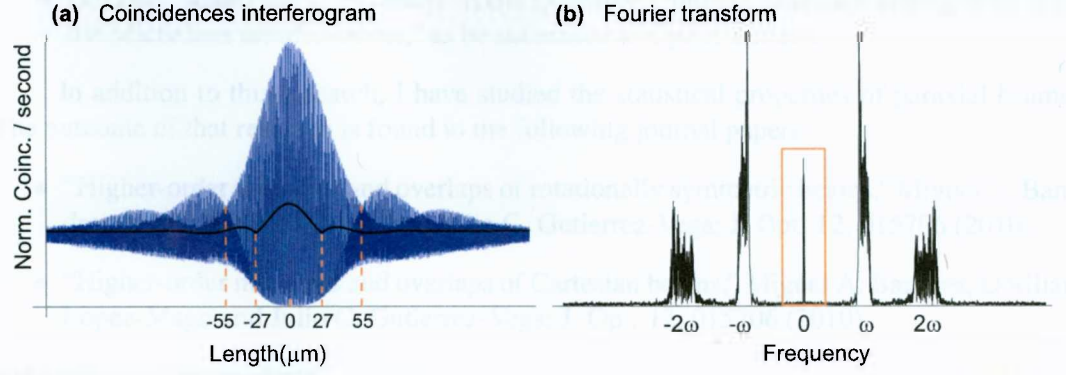
Figure 1.4: Experimental results. (a) Recorded coincidences interferogram. (b) Fourier transform of the coincidences interferogram where we have subtracted the average coincidences rate. The Fourier spectrum shows the elements predicted by Eq. (1.1). Filtering the zero frequency component, we obtain the black solid line in (a), which is the second term in Eq. (1.1). As shown in (a), the coherence length of the filtered interferogram is reduced from 55 to 27 μm, which is an enhancement in resolution by a factor of ≈ 2.

results that corroborate our theory.

This means that we can use the Michelson interferometer to implement QOCT but with the additional effort of Fourier processing the interferogram. This imposes a restriction in the implementation of this method. It requires that the spectral bandwidth of the entangled photons must be smaller than their central frequency. However, this is a minor problem since this requirement is generally satisfied.

1.4   Main Contributions

This thesis provides the theoretical background for the implementation of QOCT using a Michelson interferomter. The main contributions of this thesis are:

- The characterization of the coincidences interferogram with the two-photon Michelson interferometer using entangled photons.

- We show that the degree of entanglement between the generated photons can be measured using the coincidences interferogram.

- The conditions and procedure for the implementation of Quantum-Optical Coherence Tomography with the Michelson interferometer.

- Experimental measurements that prove our theoretical description.

The findings of this research can be found in the articles:

- D. Lopez-Mago and L. Novotny, "Coherence measurements with the two-photon Michelson interferometer," Phys. Rev. A, submitted.

- D. Lopez-Mago and L. Novotny, "Axial Quantum-Optical Coherence Tomography with the Michelson interferometer," to be submitted to Optics Letters.

In addition to this research, I have studied the statistical properties of paraxial beams. The outcome of that research is found in the following journal papers:

- "Higher-order moments and overlaps of rotationally symmetric beams," Miguel A. Bandres, Dorilian Lopez-Mago and Julio C. Gutierrez-Vega; J. Opt. 12, 015706 (2010).

- "Higher-order moments and overlaps of Cartesian beams," Miguel A. Bandres, Dorilian Lopez-Mago and Julio C. Gutierrez-Vega; J. Opt. 12, 015706 (2010).

and conference proceedings

- Lopez-Mago, D., Bandres, M. A., Gutierrez-Vega, J. C., "Propagation characteristics of Cartesian Parabolic-Gaussian beams," Proceedings of SPIE Vol. 7789, 77890Q (2010).

- Lopez-Mago, D., Bandres, M. A., Gutierrez-Vega, J. C., "Propagation of Whittaker-Gaussian beams," Proceedings of SPIE Vol. 7430, 743013 (2009).

- Burnham, D. R., Reece, P., Lopez Mago, D., et al., "Dynamics of airborne tweezing," Proceedings of SPIE Vol. 7038, 70381P (2008).

where the last proceeding came from a collaborative project with the University of Dundee, in Scotland. However, this thesis only focuses on the second part of my research work.

1.5 Thesis Organization

The thesis covers the fundamental principles of parametric down-conversion and quantum interference in the Chapter 2. Chapter 3 covers the interference of down-converted photons in the two-photon Michelson interferometer and shows experimental results. Chapter 4 explores the implementation of the two-photon Michelson interferometer in QOCT and shows the procedure for recovering the information of the layers and compare the results with the HOM interferometer. Chapter 5 provides the conclusions and future work.

Chapter 2

Theoretical Background

The quantum theory of light is the most accurate description of nature to date. It explained the blackbody radiation problem and with its development has successfully described spontaneous emission, photon-atom interactions, photodetection and nonclassical radiation. A good understanding of light phenomena requires knowledge of basic quantum theory in combination with the current state of the art in photonics technologies. The purpose of this chapter is to give a review of the underlying concepts and methods used in this thesis work. For further details refer to references [13, 14, 15, 16].

2.1 Basics of Nonlinear Optics

The response of a medium to an applied optical field is mediated by the electric polarization of the medium. The electric polarization, defined as the dipole moment per unit volume, is a function of the strength of the optical field. In linear optics, the polarization $P(t)$ depends linearly on the electric field $\tilde{P}(t) = \epsilon_0 \chi^{(1)} \tilde{E}(t)$, where ϵ_0 is the electric permittivity of free space and the constant of proportionality $\chi^{(1)}$ is known as the linear susceptibility. Nonlinear optics deals with the nonlinear response of the polarization. In this sense, the polarization is expressed as a power series expansion in the electric field:

$$\tilde{P}^{\mathrm{NL}}(t) = \epsilon_0 [\chi^{(1)} \tilde{E}(t) + \chi^{(2)} \tilde{E}^2(t) + \chi^{(3)} \tilde{E}^3(t) + \cdots], \tag{2.1}$$

which is a generalization of the linear case. The constants of proportionality $\chi^{(2)}$ and $\chi^{(3)}$ are known as the second-order and third-order nonlinear susceptibilities, respectively. In general, the susceptibilities are not scalars. They depend on the vector properties of $\tilde{E}$. Therefore, the susceptibilities become tensors, where $\chi^{(1)}$ is a second-rank tensor ($\chi_{ij}^{(1)}$), $\chi^{(2)}$ is a third-rank tensor ($\chi_{ijk}^{(2)}$), and so on. In Eq. 2.1 we assumed that the medium is dispersionless and lossless which justifies that $\tilde{P}^{\mathrm{NL}}(t)$ depends on the instant value of $\tilde{E}$. The typical values for the nonlinear susceptibilities are orders of magnitude smaller than the linear susceptibility. In order to observe nonlinear optical phenomena it is customary to use high intensity sources such as lasers.

The wave equation for a nonlinear medium is [15]:

$$\nabla^2 \tilde{E} - \frac{n^2}{c^2} \frac{\partial^2 \tilde{E}}{\partial t^2} = \frac{1}{\epsilon_0 c^2} \frac{\partial^2 P^{\mathrm{NL}}}{\partial t^2}. \tag{2.2}$$

where n is the linear refractive index and c is the speed of light in vacuum. If we compare the previous equation with the equation of a driven oscillator, the term $\partial^2 P^{\mathrm{NL}}/\partial t^2$ acts as a driving force which generates electromagnetic radiation. Then, the nonlinear terms produce electromagnetic fields with different oscillation frequencies from those of the applied electric field $\tilde{E}$. Let us review an example to illustrate the variety of nonlinear effects.

Consider that an optical field incident upon a nonlinear medium is composed of two frequencies ω_1 and ω_2 (Fig. 2.1a). The electric field is written in the form

$$\tilde{E}(t) = E_1 e^{-i\omega_1 t} + E_2 e^{-i\omega_2 t} + \mathrm{c.c.}, \tag{2.3}$$

where c.c. means complex conjugate of the previous terms. Then, taking up to the second-order susceptibility in Eq. (2.1), the nonlinear polarization is given by

$$\tilde{P}^{(2)}(t) = \epsilon_0 \chi^{(2)} \Big[E_1^2 e^{-2i\omega_1 t} + E_2^2 e^{-2i\omega_2 t} + 2E_1 E_2 e^{-i(\omega_1+\omega_2)t} +$$

$$2E_1 E_2^* e^{-i(\omega_1-\omega_2)t} + \mathrm{c.c.} \Big] + 2\epsilon_0 \chi^{(2)} \Big[|E_1|^2 + |E_2|^2 \Big]. \tag{2.4}$$

The first two terms generate electromagnetic fields at frequencies $2\omega_1$ and $2\omega_2$. This is known as second-harmonic generation (SHG). The next two terms produce radiation at frequencies $\omega_1 + \omega_2$ and $\omega_1 - \omega_2$, which are known as sum-frequency generation (SFG) and difference-frequency generation (DFG), respectively. The last term does not produce radiation, however it generates a static electric field across the nonlinear medium, known as optical rectification.

(a) Stimulated emissions

(b) Spontaneous Parametric Down-Conversion
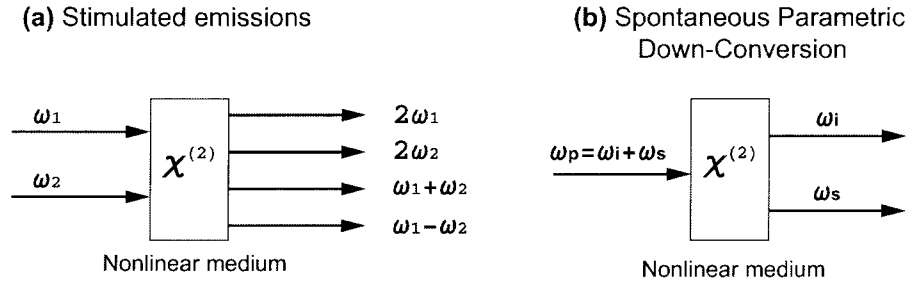
Figure 2.1: Second-order Nonlinear Processes. (a) When an electromagnetic field interacts with a nonlinear medium having a nonlinear susceptibility $\chi^{(2)}$, the resulting electromagnetic field contains second harmonics ($2\omega_1, 2\omega_2$), sum-frequency ($\omega_1+\omega_2$) and difference-frequency ($\omega_1 - \omega_2$) components. (b) In Spontaneous Parametric Down-Conversion a pump photon with frequency (ω_p) is spontaneously split into two photons with frequencies ω_i and ω_s. The down-converted photons satisfy energy conservation $\omega_s + \omega_i = \omega_p$.

The process of difference-frequency generation found many of its practical applications in the amplification of signals. For example, in optical parametric amplification a laser with frequency ω_p is used to pump a nonlinear crystal. At the same time, a small signal wave with frequency ω_s is introduce into the medium. The frequency ω_s is smaller than the frequency of the pump. Then, by means of DFG a second wave is generated at frequency $\omega_i = \omega_p - \omega_s$. This new optical field is called the idler wave. The idler wave stimulates the generation of fields

at the signal frequency ($\omega_s = \omega_p - \omega_i$). The new signal waves repeat the process. Hence, the generation of the idler wave reinforces the generation of the signal wave, and viceversa. The signal wave is exponentially amplified along the nonlinear medium in conjunction with the idler wave.

What makes the process of DFG of particular interest in this work, is the possibility of producing an entangled two-photon state. In parametric amplification, we stimulate the emission by introducing the signal wave together with the pump. However, even without the signal wave, there is the possibility that a spontaneous process creates the signal and idler fields (Fig. 2.1b). In the terminology of photons, it is not possible to say which photon becomes the idler and which photon becomes the signal. This indistinguishability generates the entanglement between the two photons. This spontaneous process is known as Spontaneous Parametric Down-Conversion (SPDC) and is reviewed in section 2.3. Before that, let us introduce the ideas behind quantum entanglement.

2.2   Introduction to Quantum Entanglement

Entanglement refers to the phenomenon where two or more particles are linked in a way that the measurement of one instantly changes the quantum state of the other, no matter how far away they are. Entanglement appeared at the early stage of quantum mechanics. Einstein, Podolsky and Rosen [17] published a seminal paper criticizing the interpretation of quantum mechanics about the wave function. In that paper they proposed a thought (''Gedanken'') experiment to probe that quantum mechanics is incomplete. They proposed that there must be some *hidden variables* which are not being taking into account. Later, John Bell showed that the predictions of hidden variable theories are in conflict with the predictions of quantum mechanics [18]. Bell developed an inequality (known as Bell's inequality) which is based on statistical measurements. Bell's inequality allowed to test the predictions of quantum mechanics versus hidden variable theories. It turned out that the experimental results agree with the quantum mechanical predictions.
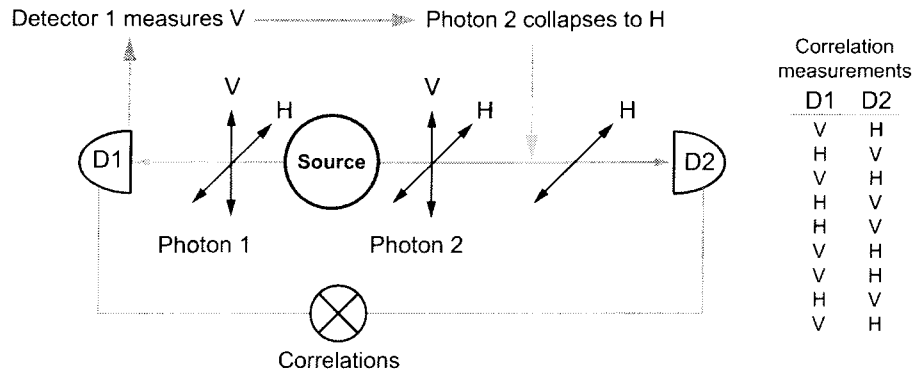

Figure 2.2: Example of polarization-entangled photons. Two photons are entangled in polarization when the detection of one photon changes the polarization state of the second photon. In this example, the entangled photons are anti-correlated.

A simple example to illustrate the idea of entanglement is shown in Fig. 2.2. There are several kinds of entangled systems. They can be atoms, ions, molecules, etc. In this particular example, we consider entanglement between photons. The entangled photons can be generated by particle collisions or by atomic transitions. The source generates two photons propagating in opposite directions. Detectors D1 and D2 measure the polarization of the photons traveling to the left and to the right, respectively. By looking at the results of each detector, we can tell that the state of the photon is a superposition of horizontal (H) and vertical (V) polarizations. In terms of quantum mechanics, the state of each photon is written as $|\varphi\rangle = (|H\rangle + |V\rangle)/\sqrt{2}$. If we measured the correlations, we would find that the photons are anti-correlated which means that whenever we get vertical polarization in D1 we get horizontal polarization in D2. The state of the system is the superposition of the states HV and VH

$$|\psi\rangle = (|H\rangle_1|V\rangle_2 + |V\rangle_1|H\rangle_2)/\sqrt{2}, \tag{2.5}$$

where the subindexes 1 and 2 refer to the detectors D1 and D2, respectively. The previous equation is what Einstein criticized about quantum mechanics. Eq. (2.5) implies that if D1 measures V polarization, the state of the second photon collapses to H even when this photon has not been detected by D2. In other words, the detection of photon 1 changes the polarization state of photon 2 and viceversa. It was probed by Bell's inequality measurements that the quantum state given in Eq. (2.5) agrees with the experimental results, excluding all the hidden variables theories.

The first experiments that demonstrated the validity of quantum mechanics were done using polarization entanglement[19, 20, 21]. The most famous is the experiment of Aspect et al. [20] which is equivalent to the example given in Fig. 2.2. In this experiment, two photons were created in an atomic cascade of calcium. Due to the angular momentum conservation, the photons are emitted in opposite directions and with orthogonal polarizations. The quantum state of the system is equivalent to Eq. (2.5) but with a different phase.

The important concepts in quantum entanglement are superposition and indistinguishability. When the possible outcomes of a process are indistinguishable, the quantum state is constructed by the superposition of each state that represents an outcome. For example, in Aspect's experiment, there is no way to tell the polarization and direction of each photon. This indistinguishability produces the superposition shown in Eq. (2.5).

After Bell's inequality [18], new criteria to test quantum entanglement were developed [22, 23, 24, 25]. Instead of deriving a Bell-type inequality, let us explain the simplest mathematical test. The general idea is to show that the combined quantum state of the system cannot be written as the product of the individual state of each particle. Suppose that a source generates photon pairs with the following quantum state:

$$|\psi\rangle = (|H\rangle_1|H\rangle_2 + |H\rangle_1|V\rangle_2 + |V\rangle_1|H\rangle_2 + |V\rangle_1|V\rangle_2)/2. \tag{2.6}$$

It is straightforward to show that the state can be factored as $|\Psi\rangle = (|H\rangle_1 + |V\rangle_1)/\sqrt{2}(|H\rangle_2 + |V\rangle_2)/\sqrt{2}$. Therefore, the state $|\Psi\rangle$ is separable or not entangled. An example of an entangled state was given by Eq. (2.5). In this case, we can see that the state cannot be factored. Then, the state is said to be inseparable or entangled. In the context of indistinguishability, the product state (2.6) means that is possible to tell the polarization of each photon before a measurement is done (notice that the two photons have diagonal polarization $|D\rangle = (|H\rangle + |V\rangle)/\sqrt{2}$).

It is important to make the distinction that, entanglement refers not to the particles themselves, but to a certain property or degree of freedom. For example, we can have two polarization-entangled photons having separable frequency states. Therefore, the indistinguishability is not associated to the particles, but to a property of the system.

For the case of photons, is possible to generate entanglement in polarization, spatial mode and energy. It is even possible to produce entanglement on each degree of freedom[26]. The general state of an entangled two-photon system is [27]:

$$|\psi\rangle = \frac{1}{\sqrt{2}}(|\alpha\rangle_1|\gamma\rangle_2 + |\beta\rangle_1|\delta\rangle_2), \tag{2.7}$$

where the $|\alpha\rangle$ and $|\beta\rangle$ are orthonormal vectors in the Hilbert space of photon 1, and $|\gamma\rangle$ and $|\delta\rangle$ likewise for photon 2. Then, the state cannot be factored into the product $|\chi\rangle_1|\xi\rangle_2$.

SPDC is one of the most versatile tools to generate photon entanglement in many degrees of freedom. SPDC is of quantum mechanical nature and in the next sections we'll review its properties.

2.3 Spontaneous Parametric Down-Conversion

The process of Spontaneous Parametric Down-Conversion is a nonlinear effect which produces pair of photons highly correlated in time of emission, frequency and momentum. It was predicted by the quantum mechanical description of optical parametric amplification [15] and was known as parametric luminescence or optical parametric noise[28]. The first to study the statistics of down-converted photons was Zel'dovich and Klyshko[29] in 1969. A year later, SPDC was experimentally demonstrated by Burnham and Weinberg [30]. The correlation properties make the two photons very attractive for testing quantum entanglement[16]. After the work of Burnham and Weinberg, entanglement in SPDC was demonstrated in many degrees of freedom, e.g. polarization, energy, linear momentum and orbital angular momentum[31].

The basic principles in the SPDC process can be understood by energy and momentum conservation (Fig. 2.3). When a nonlinear medium with a second-order susceptibility $\chi^{(2)}$ is
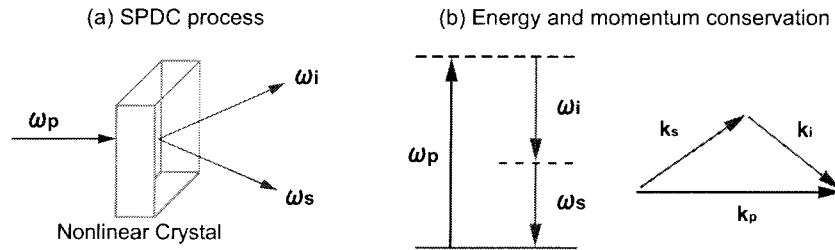
Figure 2.3: Spontaneous Parametric Down-Conversion. (a) A pump photon with frequency ω_p propagating inside a nonlinear crystal is spontaneously down-converted in two photons ω_s and ω_i. (b) Energy and momentum diagrams of a single SPDC process. The process conserves energy and momentum, which implies that the frequencies of the photons satisfy $\omega_s + \omega_i = \omega_p$ and their wavevectors $\mathbf{k}_s + \mathbf{k}_i = \mathbf{k}_p$.

pumped by a laser, with a small probability (in the order of 10^{-12}), a pump photon is split into two photons, which are called signal and idler, respectively. The process conserves the energy and momentum of the original photon, which implies the following relations in the frequencies (ω) and propagation vectors (k) of the photons:

$$\omega_p = \omega_s + \omega_i, \tag{2.8}$$

$$\mathbf{k}_p = \mathbf{k}_s + \mathbf{k}_i, \tag{2.9}$$

where p, s and i stand for pump, signal and idler. The second equation is known as the phase-matching condition and determines the spatial and spectral distribution of the down-converted photons. In materials with normal dispersion, Eqs. (2.8) and (2.9) cannot be satisfied simultaneously. This problem is overcome by using anisotropic crystals, where the refractive index n depends on the polarization of the photons. According to the polarization of the down-converted photons, there are two types of SPDC which are shown in Fig. 2.4. In Type I

(a) Type I SPDC
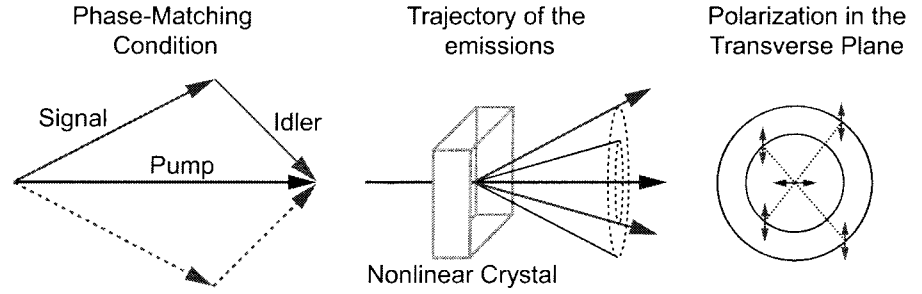
(b) Type II SPDC
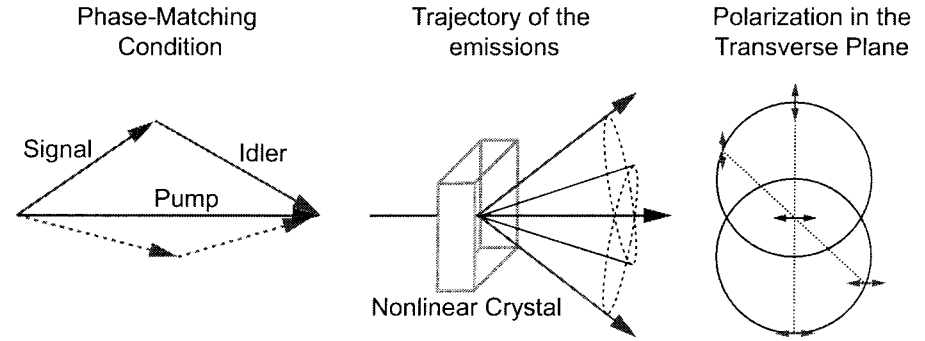
Figure 2.4: Types of Geometries in Spontaneous Parametric Down-Conversion. (a) Type I SPDC. The down-converted photons have parallel polarization but orthogonal to the pump photons. The propagation directions form two concentric cones. (b) Type II SPDC. The down-converted photons have orthogonal polarization and their propagation directions form two cones symmetrically tilted with respect to the direction of the pump photons.

SPDC the photons have the same polarization but orthogonal to the pump. The directions of

emission of the down-converted photons form two collinear cones. The cones are collinear with the optics axis defined by the pump. In the degenerate case, when the two photons have the same frequency, the cones overlap. In Type II SPDC the down-converted photons have orthogonal polarization and one of them has the same polarization than the pump photon. The trajectories of the photons define two cones whose axis are tilted with respect to the pump. The tilt lays in the plane defined by the pump and the optics axis of the anisotropic crystal. In the transverse plane, the two photons are always emitted in opposite directions, except for the particular case where they propagate collinearly with respect to the pump photon.

The magnitude of the wavevector inside the crystal is $|\mathbf{k}| = n(\omega)\omega/c$, where c is the speed of light in vacuum. The phase-matching condition in Eq. (2.9) can be rewritten as:

$$n(\omega_p)\omega_p\mathbf{p} = n(\omega_s)\omega_s\mathbf{s} + n(\omega_i)\omega_i\mathbf{i}$$ (2.10)

where the direction of the photons are indicated by the unitary vectors $\mathbf{p}$, $\mathbf{s}$, and $\mathbf{i}$. The theory of anisotropic crystals can be found in many references. For the purposes of the thesis, the case of uniaxial crystals is reviewed. For biaxial crystals, refer to Born and Wolf [14].

An uniaxial crystal supports two orthogonal propagation modes, the extraordinary and ordinary mode. The ordinary mode has refractive index $n_O(\omega)$ and polarization perpendicular to the plane of the optical axis of the crystal. The extraordinary mode has a polarization laying in the plane of the optics axis and has a refractive index which also depends on the direction of propagation. The extraordinary index of refraction has the following dispersion relation:

$$n_e(\omega, \theta) = \left[\frac{\cos^2(\theta)}{n_O^2(\omega)} + \frac{\sin^2(\theta)}{n_E^2(\omega)}\right]^{-1/2}$$ (2.11)

where θ is the angle between the optics axis and the wave vector. The limiting values of $n_e(\omega, \theta)$ are $n_e(\omega, \theta = 0) = n_O(\omega)$ (where n_O is the index of refraction for the ordinary mode) and $n_e(\omega, \theta = 90) = n_E(\omega)$. The crystal is uniaxial positive if $n_E > n_O$ and uniaxial negative if $n_E < n_O$. The values of n_O and n_E for a given frequency can be found in the literature[32]. However, their values can be approximated by the Sellmeier's equations [32, 33]:

$$n_{O,E}^2 = A + B/(\lambda^2 + C) + D\lambda^2,$$ (2.12)

where the coefficients A,B, C and D are experimentally calculated. The manufacturer of the crystal provides the values of the coefficients [34]. Using the previous equations, we can calculate the angles and frequencies that satisfy the phase-matching condition. Practically, we also need to take into account the refraction from air to crystal and the internal refraction from the crystal to air in order to calculate the angles of observation. Appendix A shows the numerical values that were calculated in this work. There is a geometrical solution to the problem, which is useful to understand the symmetries of the two types of SPDC.

2.3.1 Geometrical interpretation

For a fixed frequency, the dispersion relation $|\mathbf{k}| = n(\mathbf{k})\omega/c$ is the equation of a surface in the $\mathbf{k}$-space, known as the $\mathbf{k}$-surface. Each mode has its respective $\mathbf{k}$-surface. The intersection of the wavevector $\mathbf{k}$ with the $\mathbf{k}$-surfaces determines the values of n_O and n_e. To visualize this

idea, refer to Fig. 2.5, where we can see the plane (k_z, k_x) for negative and positive uniaxial crystals. The optics axis of the crystal is the direction of k_z. The surfaces intersect this plane in an ellipse and a circle. The circle corresponds to the ordinary mode and the ellipse to the extraordinary mode. Consider that the wave vector have a direction u forming an angle θ with respect to the optics axis. The intersection of u with the circle gives the value of $|k_o|$ and the intersection with the ellipse gives the value of $|k_e|$. With this interpretation, we see that for a fixed frequency, the refractive index of the extraordinary mode change with the angle of propagation. The two modes share the same index of refraction when the wave propagates parallel to the optics axis. Using this interpretation, we can now observe how to satisfy the
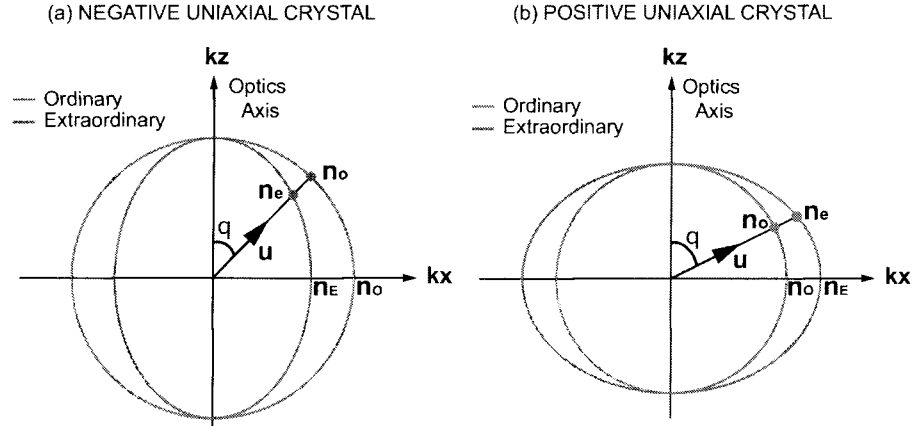
Figure 2.5: k-Surfaces in uniaxial crystals. An electromagnetic wave propagating inside an uniaxial crystal has two propagation modes. The propagation plane is defined by the optics axis of the crystal and the propagation direction u. The ordinary mode has polarization orthogonal to the propagation plane whereas the extraordinary mode has parallel polarization. The intersection of the line with direction u with the k-surfaces defines the values of the refractive indexes n_o and n_e for the extraordinary and ordinary modes, respectively. (a) In a negative uniaxial crystal $n_e < n_o$. (b) In a positive uniaxial crystal $n_e > n_o$.

phase-matching condition. Refer to Fig. 2.6. It is convenient to choose the polarization of the pump in the extraordinary mode. In this way, we can control the angle of emission by rotating the crystal. Since we can control the angle between the optics axis and the pump, the solution for $|k_p|$ is found by the intersection with the k-surface. For the down-converted photons, we trace the k-surface of each one in the same plane. The origin of one of the surfaces is placed at the end of k_p. The solution of the phase-matching equation is given by the intersection of the two surfaces. In Type I SPDC the k-surface is given by the ordinary mode which form a circle in the (k_z, k_x) planes. We can see that the intersection of the two circles in Fig. 2.6a produces two solutions which are symmetrically oriented with respect to the pump beam. If we consider the complete space, we have spheres instead of circles for the k-surfaces. The intersection of the circles define the two cones shown in Fig. 2.4a. For Type II, one of the k-surfaces corresponds to the extraordinary mode. In this case, the intersection of the ellipse with the circle produces two solutions which are asymmetric with respect to the pump (Fig.

2.6b). In the same way, if we consider the 3D-space, the intersection of the ellipsoid with the sphere form the two tilted cones shown in Fig. 2.4b.
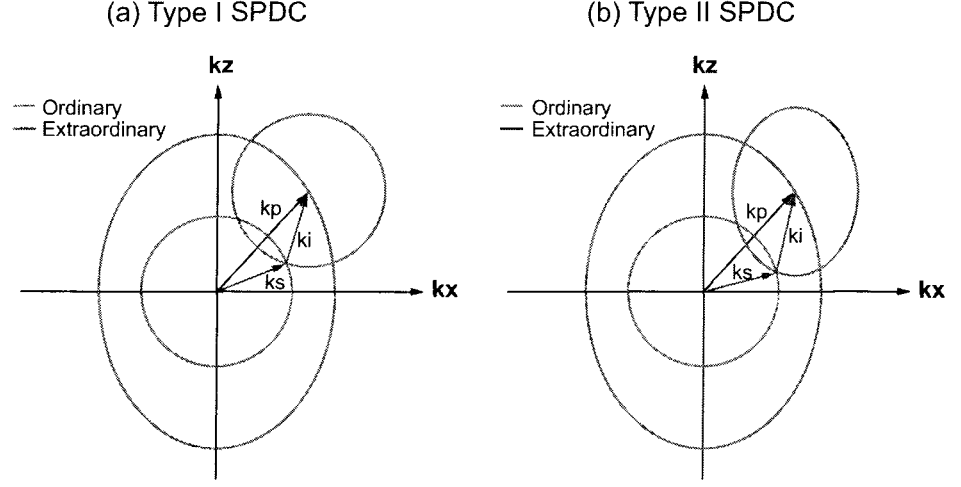
Figure 2.6: Geometrical interpretation of the phase-matching condition. The solution of the phase-matching condition is the intersection of the k-surfaces produced by the down-converted photons. (a) In Type I SPDC the solution is the intersection of two circles, which in the 3D-space form the concentric cones in Fig. 2.4a. (b) In type II SPDC the solution corresponds to the intersection of an ellipse and a circle which produces the tilted cones shown in Fig. 2.4b.

2.3.2 Quantum Mechanical Description of SPDC

A first approach to study the process of SPDC is to consider the interaction Hamiltonian with the signal and idler fields having two possible modes [13]:

$$\hat{H}_I = i\hbar g_1 \hat{a}_\alpha^{(s)} \hat{a}_\gamma^{(i)} + i\hbar g_2 \hat{a}_\beta^{(s)} \hat{a}_\delta^{(i)} + H.c., \tag{2.13}$$

where H.c. stands for Hermitian conjugate of the previous terms. $\hat{a}^{(s)}$ and $\hat{a}^{(i)}$ are the annihilation operator for the signal and idler fields, respectively. The constants g_1, g_2 are related to the second-order susceptibility $\chi^{(2)}$ and the properties of the pump. The pump is treated as a classical field. In the interaction picture, the quantum state evolves as

$$|\psi(t)\rangle = \exp(-i\hat{H}_I t/\hbar)|\psi(0)\rangle. \tag{2.14}$$

The efficiency of photon generation is proportional to $\eta_{1,2} = |g_{1,2}\tau|$, where τ is the interaction time of the process. Generally, the efficiency is in the order of $\sim 10^{-12}$ (one photon pair is generated for each 10^{12} photons). Expanding the exponential in Eq. (2.14) and taking the initial state as the vacuum, the state becomes

$$|\psi\rangle \approx \eta_1|\alpha\rangle|\gamma\rangle + \eta_2|\beta\rangle|\delta\rangle. \tag{2.15}$$

This final state, means that, if we measure one of the photons and find that is in the mode α, the other photon is in the mode γ and this happens with probability η_1. The same argument holds for the second term. The modes α and β are orthogonal as well as the modes γ and δ. For example, if we consider that the mode $\alpha \equiv H$ (so $\beta \equiv V$) and $\gamma \equiv V$ ($\delta \equiv H$), we arrive at the entangled state given in Eq. (2.5).

In general, the process of SPDC produces entanglement in the energy degree of freedom. The polarization entanglement is usually engineered by using additional elements (which means that the state becomes entangled in two degrees of freedom). For the frequency degree of freedom, the state in Eq. (2.15) can be written as

$$|\psi\rangle \approx \eta_1 |\omega_1\rangle_s |\omega_2\rangle_i + \eta_2 |\omega_2\rangle_s |\omega_1\rangle_i. \tag{2.16}$$

where the energy conservation Eq. (2.8) implies that $\omega_1 + \omega_2 = \omega_p$. It is clear that Eq. (2.16) represents a frequency-entangled state.

2.4 One-photon and two-photon interference

The double-slit experiment by Thomas Young started the study of interference. Despite its long history, interference still remains to challenge our understanding. Feynman referred to interference as the only mystery of quantum mechanics. The Feynman's rules of interference are [35]:

1. The probability P of a particular outcome from the interaction of a particle with an apparatus is given by the square of the absolute value of a complex probability amplitude f.

$$
\begin{aligned}
P &= \text{Probability}, \\
f &= \text{Probability amplitude}, \\
P &= |f|^2. \tag{2.17}
\end{aligned}
$$

2. When the same outcome can occur in *indistinguishable* alternative ways, the probability amplitude is the sum of the probability amplitudes for each way considered separately. **There is interference**. For example:

$$
\begin{aligned}
f &= f_1 + f_2, \\
P &= |f_1 + f_2|^2. \tag{2.18}
\end{aligned}
$$

3. If an experiment is performed which is capable of determining whether one or another alternative is actually taken, the probability of the event is the sum of the probabilities for each alternative. **The interference is lost**.

$$P = P_1 + P_2. \tag{2.19}$$

We proceed to apply the rules of interference for optical experiments. In optical experiments, light coming from several sources is allowed to come together and mix, and the

resulting light intensity is measured at various positions. The interference is characterized by the phase difference between the sources. However, according to Feynman's rules of interference, the interference is lost when the different pathways of the light are distinguishable.

The principles of quantum optical interference can be generalized as follows [36]. Consider two fields produced by the sources S_A and S_B, as shown in Fig. 2.7. A detector $D1$ is used repeatedly to measure the probability $P_1(x_1)$ of detecting a photon in a short time interval as a function of position x_1. From the source S_A (S_B) to detector $D1$ the photon acquires a phase ϕ_{A1} (ϕ_{B1}). Then, the probability *amplitude* of the photon coming from S_A (S_B) is $f_A(\phi_{A1})$ ($f_B(B1)$). If the sources are indistinguishable, according to the Feynman's rules of interference, we sum the probabilities amplitudes f_A and f_B and the resulting probability is $P = |f_A(\phi_{A1}) + f_B(\phi_{B1})|^2$. The interference is characterized by the phase difference $\phi_{A1} - \phi_{B1}$. On the other hand, if we can tell from which source the photon comes, the interference is lost and the resulting probability is $P = |f_A(\phi_{A1})|^2 + |f_B(\phi_{B1})|^2$. Because the probability depends on the second power of the optical field and on the detection of one photon at a time, this kind of experiments are called second-order or one-photon interference.
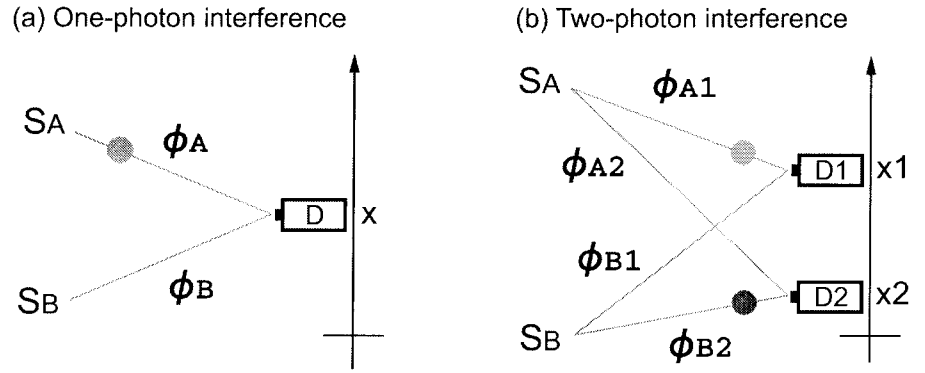
Figure 2.7: (a) One-photon interference. Detector D measures the probability of detecting a photon as a function of position x. (b) Two-photon interference. Detectors D1 and D2 measure the probability of detecting one photon in x_1 and a second photon in x_2.

Two photodetectors $D1$ and $D2$ working in coincidences measure the *joint* probability $P_2(x_1, x_2)$ of detecting one photon at position x_1 and a second photon at x_2. In this case, the probability P_2 depends on the fourth power of the field, and hence we call this kind of experiments fourth-order or two-photon interference. The interference is characterized by the phase differences $\phi_{A1} - \phi_{B1}$ and $\phi_{A2} - \phi_{B2}$.

We remark that the quantum interference is not the interference between particles (photons in this case). In one-photon interference, only the probability amplitudes of the same photon interfere with each other. In the case of two-photon interference, the probability amplitudes of the photon pairs interfere with each other.

The central component in all the interference experiments is the optical beam splitter. In the classical wave picture, the effect of the beam splitter can be understood as the splitting of the incoming wave into a reflected and a transmitted partial wave. Each of these waves contains half the energy (Fig. 2.8a). However, the process of splitting becomes conceptually

difficult in the photon picture.

(a) The wave picture   (b) The photon picture

Figure 2.8: Wave and photon pictures of the 50:50 beam splitter. (a) In the wave picture an incident electromagnetic wave is split in two electromagnetic waves containing half its energy. (b) In the photon picture an incident photon is split into two "virtual" photons. The probability of detecting a virtual photon is 1/2. However, detecting one of the virtual photons cancels the probability of detecting the other virtual photon.

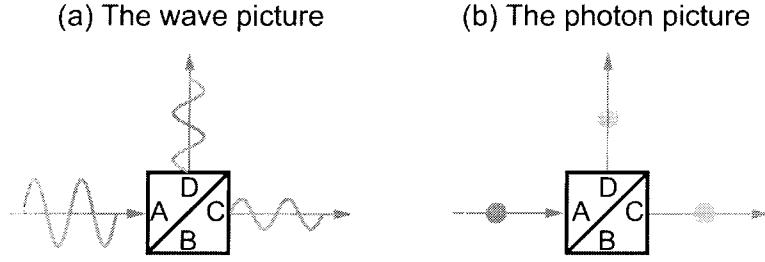Let us represent a monochromatic photon with angular frequency ω entering the beam splitter through the input port A as $|\omega, a\rangle$ (Fig. 2.8b). The beam splitter transforms an initial quantum state $|\psi\rangle_{in} = |\omega, a\rangle$ into

$$|\psi\rangle_{out} = r|\omega, d\rangle + t|\omega, c\rangle, \qquad (2.20)$$

where r, t are the reflection and transmission coefficients (for a perfect 50:50 beam splitter, $r = i/\sqrt{2}$ and $t = 1/\sqrt{2}$). The states $|\omega, c\rangle$ and $|\omega, d\rangle$ represents the output ports C and D, respectively. This means that with a probability of $|r|^2$ the photon can be found in C and with probability $|t|^2$ the photon can be found in D.

2.4.1 The one-photon Michelson interferometer

Let us review the one-photon Michelson interferometer in the context of quantum mechanics (Fig. 2.9). Consider a photon wavepacket state written as a weighted superposition of monochromatic modes

$$|\psi\rangle_{in} = \int d\omega \phi(\omega)|\omega, a\rangle, \qquad (2.21)$$

with $\phi(\omega)$ being the probability amplitude of the state $|\omega\rangle$. The spectral density $\Phi(\omega) = |\phi(\omega)|^2$ is normalized ($\int \Phi(\omega) d\omega = 1$), has a central frequency $\bar{\omega}$ and bandwidth $\Delta\omega$ at full width at half maximum (FWHM).

The beam splitter transforms each monochromatic mode according to the Eq. (2.20). $|\omega, d\rangle$ evolves along path 1 and acquires a phase $\exp(i\omega t_1)$. After exiting the beam splitter through output port B becomes $|\omega, d\rangle \rightarrow t \exp(i\omega t_1)|\omega, b\rangle$. In the same way, $|\omega, c\rangle$ acquires a phase $\exp(i\omega t_2)$ and at the output port B $|\omega, c\rangle = r \exp(i\omega t_2)|\omega, b\rangle$. Then, the wavepacket state after the Michelson interferometer is

$$|\psi\rangle_{out} = rt \int d\omega \phi(\omega)(1 + e^{i\omega\tau})|\omega\rangle, \qquad (2.22)$$

where $\tau = t_2 - t_1$. For simplicity we discarded the label of the spatial mode b.

A photodetector works by photon absorption which doesn't distinguish between the different frequency components (we are assuming a perfect photodetector, in reality, the absorption efficiency depends on the frequency). Therefore, the probability P of detecting a wavepacket state is $P = \int d\omega' |\langle \omega' | \psi \rangle|^2$, where the integration is over the monochromatic modes that enter the photodetector.

The probability of detecting the state 2.22 is

$$P(\tau) \propto 1 + \Gamma(\tau)\cos(\overline{\omega}\tau). \tag{2.23}$$

In the derivation we used the orthogonality condition $\langle \omega' | \omega \rangle = \delta(\omega' - \omega)$. The function $\Gamma(\tau) = \int d\omega', \Phi(\omega' + \overline{\omega})\cos(\omega'\tau)$ corresponds to the Fourier transform of the spectral density.

The interferogram $P(\tau)$ features two contributions: a DC term and an interference term. The DC term is the average number of single counts or average intensity. The interference term produces fringes with oscillation frequency $\overline{\omega}$ which are modulated by $\Gamma(\tau)$. Practically, we can relate τ to the path-length difference $x = 2(l_2 - l_1)$ through $\tau = x/c$ where l_1 and l_2 are the lengths of the interferometer arms and c is the speed of light. The half width at half maximum of $\Gamma(x)$ defines the coherence length L_c, i.e. $\Gamma(L_c) = \frac{1}{2}\Gamma_{max}$. The coherence length depends on the shape of $\Phi(\omega)$, however, as a rule of thumb $L_c \approx c/\Delta\omega$. In experiments, $\Gamma(x)$ is the visibility V of the fringes, given by

$$V = \frac{P_{max} - P_{min}}{P_{max} + P_{min}} = \frac{I_{max} - I_{min}}{I_{max} + I_{min}}, \tag{2.24}$$

with I_{max} and I_{min} being the maximum and minimum intensities of the fringes. For illustration, we consider a spectral density with a Gaussian distribution. The resulting interference pattern is shown in Fig. 2.9b.

(a) One-photon Michelson interferometer   (b) Interference pattern
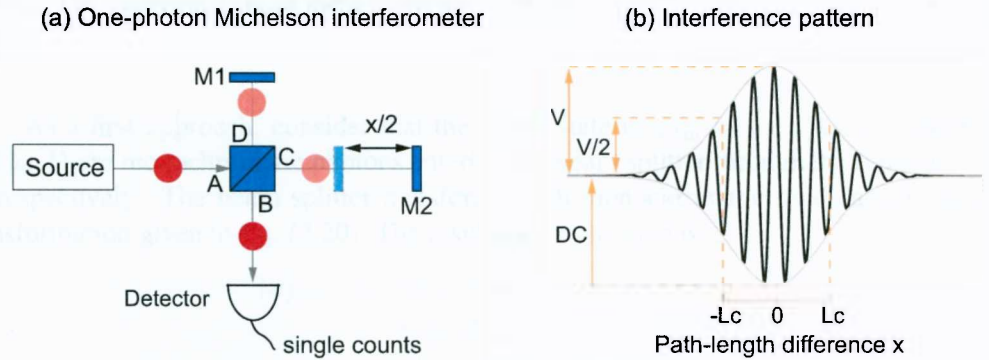
Figure 2.9: (a) Schematic of the one-photon Michelson interferometer. M: mirror, x: path-length difference between the interferometer arms, A-D: ports of the beam splitter. We assume that the spectral density $\Phi(\omega)$ of the source has a Gaussian distribution. (b) Interference pattern. V: visibility, L_c: coherence length, DC: average intensity. The coherence length is the distance where the visibility of the fringes decreases half of its maximum.

2.4.2 The Hong-Ou-Mandel interferometer

Let us review the two-photon Hong-Ou-Mandel (HOM) interferometer [9]. The HOM interferometer, shown in Fig. 2.10, involves a pair of down-converted photons entering a beam splitter from two separate input ports. Because of the involvement of two photons, there are four possibilities for the output of the beam splitter: both are transmitted, both are reflected, and one is transmitted while the other is reflected (Fig. 2.10b). The first two possibilities are indistinguishable, resulting in the addition of their probability amplitudes. However, because of the π-phase difference given when both photons are reflected, the amplitude addition leads to destructive interference, and the two cases completely cancel each other when their amplitudes are the same.

(a) Hong-Ou-Mandel interferometer   **(b) Four possible scenarios**
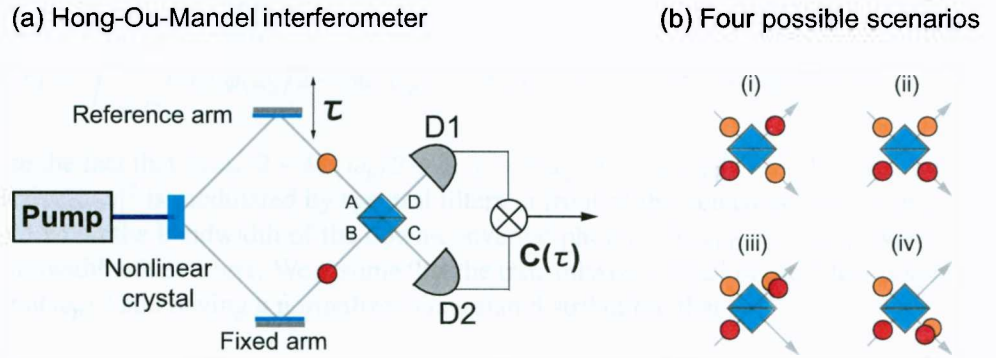
Figure 2.10: (a) Schematic of the Hong-Ou-Mandel interferometer. Two down-converted photons enters a beam splitter through input ports A and B. Two photodetectors, D_1 and D_2 working in coincidences measure the coincidences counts $C(\tau)$ as a function of the time delay τ introduced in the reference arm. (b) The photon pairs have four possibilities to exit the beam splitter. The superposition of these possibilities produces the interference in the coincidences rate.

As a first approach, consider that the initial state is $\psi\rangle_{\text{in}} = |\omega, a\rangle|\omega, b\rangle$, where $|\omega, a\rangle$ and $|\omega, b\rangle$ are monochromatic photons entering the beam splitter through the input port A and B, respectively. The beam splitter transforms each monochromatic mode according to the transformation given in Eq. (2.20). The resulting output state is

$$
\begin{aligned}
|\psi\rangle_{\text{out}} &= rt|\omega, d\rangle|\omega, d\rangle + tr|\omega, c\rangle|\omega, c\rangle \\
&+ r^2|\omega, d\rangle|\omega, c\rangle + t^2|\omega, c\rangle|\omega, d\rangle.
\end{aligned}
\tag{2.25}
$$

The first two terms are the cases *i* and *ii* in Fig. 2.10b. The last two terms are the cases *iii* and *iv* and they contribute to the coincidences. Since they are indistinguishable, the probability of detecting a coincidence is $P = |r^2 + t^2|^2$. For a 50:50 beam splitter $r = i/\sqrt{2}$ and $t = 1/\sqrt{2}$ and $P = 0$.

In practice, the down-converted photons are never monochromatic. Let us represent the multimode two-photon state as the coherence superposition

$$
|\psi\rangle_{\text{in}} = \int_0^{\omega_p} d\omega \phi(\omega, \omega_p - \omega)|\omega, a\rangle|\omega_p - \omega, b\rangle,
\tag{2.26}
$$

where $\phi(\omega_1, \omega_2)$ is a weighting function peaked at $\omega_1 = \omega_2 = \omega_p/2$, ω_p is the frequency of the pump source and $\omega_1 + \omega_2 = \omega_p$. We assume a monochromatic pump laser. Eq. 2.26 is the generalization of Eq. (2.16). The reference arm introduces a time delay τ and $|\omega, a\rangle$ acquires a phase $\exp(i\omega\tau)$. In the same manner as before, the beam splitter transforms the state $|\omega, a\rangle|\omega_p - \omega, b\rangle$ as given in Eq. 2.25. Keeping the terms that contribute to the coincidences and considering the phase delay in the input port A, the output state is

$$|\psi\rangle_{\text{in}} = \int_0^{\omega_p} \mathrm{d}\omega \phi(\omega, \omega_p - \omega) e^{i\omega\tau} (r^2 |\omega, d\rangle |\omega_p - \omega, c\rangle + t^2 |\omega, c\rangle |\omega_p - \omega, d\rangle). \qquad (2.27)$$

Notice that the terms where $\omega = \omega_p/2 - \delta\omega$ and $\omega = \omega_p/2 + \delta\omega$ are indistinguishable, i.e. $|\omega_p/2 - \delta\omega, d\rangle |\omega_p/2 + \delta\omega, c\rangle$ and $|\omega_p/2 + \delta\omega, c\rangle |\omega_p/2 - \delta\omega, d\rangle$. The coincidences rate $C(\tau)$ is

$$C(\tau) = \int_{-\omega_p/2}^{\omega_p/2} \mathrm{d}\delta\omega |\phi(\omega_p/2 - \delta\omega, \omega_p/2 + \delta\omega)|^2 |r^2 e^{i(\omega_p/2 - \delta\omega)\tau} + t^2 e^{i(\omega_p/2 + \delta\omega)\tau}|^2. \qquad (2.28)$$

We use the fact that $\phi(\omega_p/2 - \delta\omega, \omega_p/2 + \delta\omega) = \phi(\omega_p/2 + \delta\omega, \omega_p/2 - \delta\omega)$. Then, we assume that $|\phi(\omega_1, \omega_2)|^2$ is modulated by spectral filters in front of the detectors. This approximation is valid when the bandwidth of the down-converted photons $\Delta\omega_{\text{SPDC}} > \Delta\omega_f$, where $\Delta\omega_f$ is the bandwidth of the filters. We assume that the transmissivity $F(\omega)$ of the filters is symmetric, center at $\omega_p/2$ and having a normalized Gaussian distribution, that is

$$F(\omega) = \frac{1}{\sqrt{2\pi\sigma^2}} \exp\left(-\frac{(\omega - \omega_p/2)^2}{2\sigma^2}\right), \qquad (2.29)$$

with $\sigma = \Delta\omega_f/2\sqrt{2\ln(2)}$ being the standard deviation and $\Delta\omega_f$ the full width at half maximum. Finally, substituting $|\phi|^2 = F(\omega_p/2 + \delta\omega)$ in Eq. (2.28) and considering a 50:50 beam splitter ($r = i/\sqrt{2}$ and $t = 1/\sqrt{2}$), the coincidences rate or fourth-order interferogram becomes

$$C(\tau) \propto 1 - \exp\left(-2\sigma^2\tau^2\right). \qquad (2.30)$$

The interferogram is shown in Fig. 2.11 which contains a dip when $\tau = 0$. The dip is known as the HOM dip and was experimentally demonstrated by Hong et al. [9]. Compared to the Michelson interferogram, the HOM interferogram contains two important characteristics:

- Because of the frequency correlations, the interferogram doesn't contain fringes. In addition, as we will see in Chapter 4, the interferogram is not affected by frequency dispersion.

- The coherence length of the dip is half the coherence length of the Michelson interferogram. This means that the HOM interferogram produces an enhancement in axial resolution by a factor of 2.

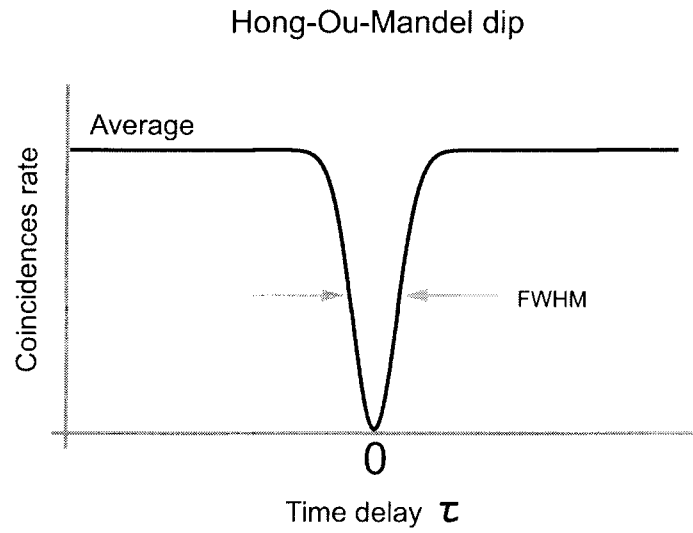The next chapter analyzes the characteristics of the two-photon Michelson interferometer.

Figure 2.11: Coincidences interferogram for the HOM interferometer. The interferogram traces out a dip when both photons travel the same optical path length ($\tau = 0$). The coherence length (FWHM/2) of the HOM dip is half the coherence length given in a Michelson interferometer.

Chapter 3

The Two-Photon Michelson Interferometer

This chapter describes the properties of the two-photon Michelson interferometer. We start discussing the working principles by considering a monochromatic approach. Then, we extend the theory to include the spectral properties of the SPDC process. Finally, we show experimental results that prove our theoretical predictions.

The two-photon Michelson interferometer is shown in Fig. 3.1a. It makes use of a source of photon pairs. At the output of the interferometer, we measure the two-photon state by using a second beam splitter and two photodetectors working in coincidences. The introduction of the second beam splitter decreases the coincidences rate by half, but doesn't change the interference pattern. Interference in the coincidences rate occurs because of the different ways the photon pairs can propagate through the interferometer.

Consider that a pair of photons enter the beam splitter through the input port A. The photon pairs can exit the Michelson interferometer by four different ways: both photons are transmitted and then reflected, both photons are reflected and then transmitted or one photon is transmitted/reflected and the second photon is reflected/transmitted (Fig. 3.1b). The indistinguishability of these scenarios gives rise to interference in the coincidence counts.

Consider the input state given by the product of two monochromatic modes $|\psi\rangle_{in} = |\omega_1\rangle|\omega_2\rangle$. The photon pairs enter the beam splitter through the input port A. After the interferometer, each monochromatic mode becomes $|\omega\rangle \rightarrow rt \exp(i\omega t_1) + tr \exp(i\omega t_2)$ where t_1 is the time required to travel the reference arm whereas t_2 is the time required to travel the fixed arm, r and t are the reflection and transmission coefficients of the beam splitter, respectively. The final state

$$|\psi\rangle_{out} = r^2 t^2 (e^{i\omega_1 t_1} e^{i\omega_2 t_1} + e^{i\omega_1 t_2} e^{i\omega_2 t_2} + e^{i\omega_1 t_1} e^{i\omega_2 t_2} + e^{i\omega_1 t_2} e^{i\omega_2 t_1}) |\omega_1\rangle|\omega_2\rangle, \qquad (3.1)$$

is equivalent to the four scenarios given in Fig. 3.1b. This approximation, however, is not suitable for differentiating between entangled and separable states.

The interference pattern depends on the correlation between the two photons. If the two photons are not entangled, the interference pattern is the product of two single-photon interferograms (refer to Fig. 2.9). If the photons are entangled, the interference pattern reflects the degree of entanglement. Therefore, by recording the interferogram we can measure the degree of entanglement between the photon pairs.

(a) Two-Photon Michelson interferometer   (b) Four different scenarios
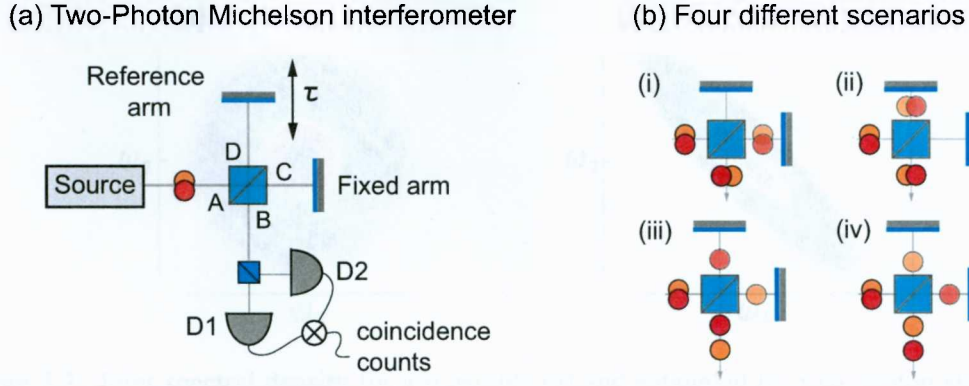

Figure 3.1: (a) The two-photon Michelson interferometer. The interferometer uses a source of photon pairs. The detection of the photon pairs is implemented by two photodetectors, D_1 and D_2 working in coincidences. The coincidences rate $C(\tau)$ is a function of the delay time τ introduced by the reference arm. (b) The interference of the coincidences rate occurs because the photon pairs can exit the interferometer by four different ways: both photons are transmitted and then reflected (i), both are reflected and then transmitted (ii) or one photon is transmitted/reflected and the second photon is reflected/transmitted (cases iii and iv).

Let us distinguish between separable and entangled states. The join state of two photons can be written as

$$|\psi\rangle = \int\int d\omega_1 d\omega_2 \phi(\omega_1, \omega_2)|\omega_1\rangle|\omega_2\rangle, \tag{3.2}$$

where $\phi(\omega_1, \omega_2)$ is the joint probability amplitude. The joint spectral density $\Phi(\omega_1, \omega_2) = |\phi(\omega_1, \omega_2)|^2$ is the probability of detecting one photon with frequency ω_1 and the second photon with frequency ω_2. If $\phi(\omega_1, \omega_2)$ can be factored into separate functions of ω_1 and ω_2 the state $|\psi\rangle$ is separable, otherwise it is entangled.

A separable state can be expressed as the product of two photons $|\psi\rangle = |\psi_1(\omega_1)\rangle|\psi_2(\omega_2)\rangle$ and the joint spectral density becomes $\Phi(\omega_1, \omega_2) = \Phi_1(\omega_1)\Phi_2(\omega_2)$. On the contrary, an entangled state cannot be factored and $\Phi(\omega_1, \omega_2)$ is a function which depends on the correlation between ω_1 and ω_2. In the plane (ω_1, ω_2) the joint spectral density is symmetric for a separable state and asymmetric for an entangled state (Fig. 3.2).

Let us now to consider the multi-mode representation of the SPDC process. For the purpose of this work, we consider degenerate Type I down-converted photons in collinear propagation. The joint spectral density $\Phi(\omega_1, \omega_2)$ of the down-converted photons depends on the pump spectral density $P(\omega) = |p(\omega)|^2$ and the physical properties of the crystal. In what follows, $P(\omega)$ has a FWHM bandwidth $\Delta\omega_P$ and central frequency $\overline{\omega}_P$. The joint probability amplitude $\phi(\omega_1, \omega_2)$ has been calculated by Ou [16] as

$$\phi(\omega_1, \omega_2) = \int d\omega_3 p(\omega_3)h(\omega_1, \omega_2, \omega_3)\delta(\omega_1 + \omega_2 - \omega_3), \tag{3.3}$$

$$h(\omega_1, \omega_2, \omega_3) = \text{sinc}(\Delta K L/2), \tag{3.4}$$

with $h(\omega_1, \omega_2, \omega_3)$ being the phase-matching function ($\text{sinc}(x) = \sin(x)/x$) and $\Delta K =$
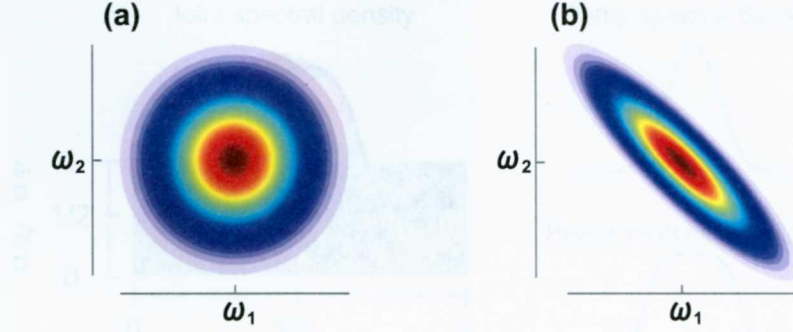
Figure 3.2: Joint spectral density for a separable (a) and entangled (b) two-photon state. In this example, the entangled photons are anti-correlated.

$[n_e(\omega_3)\omega_3 - n_o(\omega_1)\omega_1 - n_o(\omega_2)\omega_2]/c$ is the phase matching condition for an uniaxial crystal with extraordinary and ordinary index of refraction, n_e and n_o, respectively, and L is the length of the crystal. Notice that $\delta(\omega_1 + \omega_2 - \omega_3)$ comes from the energy conservation. After integrating over the delta function in Eq. (3.3), the joint spectral density can be written as

$$\Phi(\omega_1, \omega_2) = P(\omega_1 + \omega_2)H(\omega_1, \omega_2). \tag{3.5}$$

where $H(\omega_1, \omega_2) = |h(\omega_1, \omega_2, \omega_1 + \omega_2)|^2$. The function H is equivalent to a bandpass function with bandwidth $\Delta\omega_H$ and central frequency $\overline{\omega}_H = \overline{\omega}_P/2$. $\Delta\omega_H$ is typically very broad, in the order of $10^{12\sim13}$ Hz. We will show that the degree of entanglement is proportional to $\gamma = \Delta\omega_H/\Delta\omega_P$. Therefore, the degree of entanglement is in general higher when using a CW laser than a pulsed laser (since $\Delta\omega_P^{(pulsed)} >> \Delta\omega_P^{(cw)}$).

Figure 3.3 shows the joint spectral density of Type I down-converted photons. We assume that the spectrum of the pump photons $P(\omega)$ is Gaussian. For a narrow pump bandwidth the spectrum is concentrated along the line $\omega_1 + \omega_2 = \overline{\omega}_P$, on the other hand, for a large pump bandwidth the spectrum is smeared out and the degree of entanglement is considerably reduced.

In experiments, the detection of photon pairs is accomplished by two photodetectors working in coincidences. Optical bandpass filters are introduced in front of the detectors to reduce the background noise. However, the filters also modify the joint spectral density by selecting a region in the plane (ω_1, ω_2). Consider that $F_1(\omega_1)$ and $F_2(\omega_2)$ are the spectral transmissivities of the filters in detection paths 1 and 2, respectively. The joint spectral density becomes

$$\Phi(\omega_1, \omega_2) \rightarrow F_1(\omega_1)F_2(\omega_2)\Phi(\omega_1, \omega_2). \tag{3.6}$$

Let us write the state of the down-converted photons substituting Eq. (3.3) into Eq. (3.2) and integrating over ω_2, which produces

$$|\psi\rangle = \int\int d\omega_1\omega_3\phi(\omega_1, \omega_3 - \omega_1)|\omega_1\rangle|\omega_2\rangle. \tag{3.7}$$

Then, we assume that in the region defined by the bandpass filters, the phase matching function $H \approx 1$. This is valid if $\Delta\omega_F < \Delta\omega_H$, where $\Delta\omega_F$ is the bandwidth of the filters at
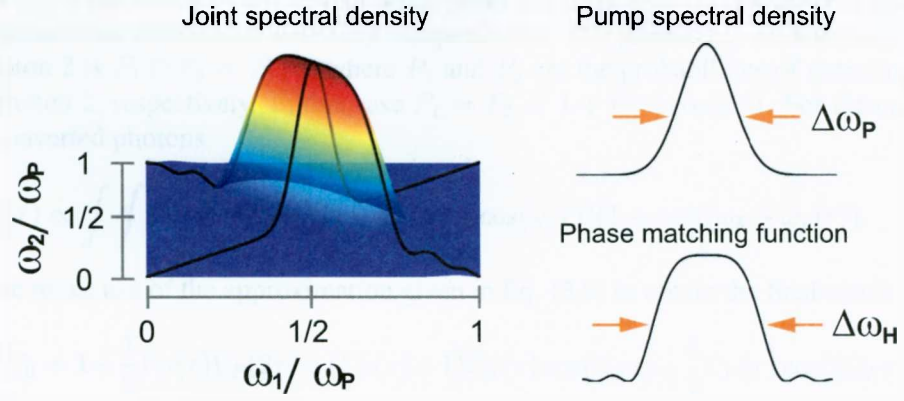
Figure 3.3: Joint spectral density $\Phi(\omega_1, \omega_2)$ for type I down-converted photons. $\Phi(\omega_1, \omega_2)$ is proportional to the pump spectral density $P(\omega)$ and the phase matching function $H(\omega_1, \omega_2)$ of the crystal. The degree of entanglement is related to the ratio $\gamma = \Delta\omega_H/\Delta\omega_P$ where $\Delta\omega_P$ and $\Delta\omega_H$ are the bandwidths of the pump laser and the phase matching function, respectively.

FWHM. This assumption is satisfied in most of the experiments that used CW lasers as the pump source. For pulsed lasers, however, we need to calculated the phase matching function. Furthermore, the filter bandwidth is larger than the linewidth of the pump laser, which yields $\omega_P < \Delta\omega_F < \Delta\omega_H$. We consider that the bandpass filters have the following normalized spectral transmissivity

$$F(\omega) = \begin{cases} 1/\Delta\omega_F & |\omega - \overline{\omega}_F| < \Delta\omega_F/2 \\ 0 & |\omega - \overline{\omega}_F| > \Delta\omega_F/2 \end{cases}, \tag{3.8}$$

where the central frequency $\overline{\omega}_F = \overline{\omega}_P/2$. Making use of the symmetry of the bandpass filters $F(\omega_1) = F(\omega_3 - \omega_1)$ and $F(\omega) \propto F^2(\omega)$ allows us to rewrite the joint spectral density in the compact form

$$\Phi(\omega_1) \approx P(\omega_3)F(\omega_1). \tag{3.9}$$

Thus, the joint spectral density and hence the degree of entanglement can be controlled with two experimental parameters: the bandwidth of the pump laser and the bandwidth of the bandpass filters.

We proceed to analyze the complete coincidence interferogram $C(\tau)$ of the two-photon Michelson interferometer by taking into account the spectral distribution. The output state in Eq. (3.1) can be generalized as

$$|\psi\rangle \propto \int \int d\omega_1 d\omega_2 \phi(\omega_1, \omega_2)(1 + e^{i\omega_1\tau})(1 + e^{i\omega_2\tau})|\omega_1\rangle|\omega_2\rangle, \tag{3.10}$$

where $\tau = t_2 - t_1$ is the time difference between the interferometer arms (introduced by the reference arm). As mentioned before, when the state is separable the coincidence interferogram can be written as

$$C(\tau) \propto (1 + \Gamma(\tau)\cos(\overline{\omega}\tau))^2, \tag{3.11}$$

where $\Gamma(\tau)$ is the Fourier transform of $\Phi(\omega)$ [refer to Eq. (2.23)]. This separable state can be easily understood in terms of statistical independence. The probability of detecting photon 1 *and* photon 2 is $P_1 \cap P_2 = P_1 P_2$, where P_1 and P_2 are the probabilities of detecting photon 1 and photon 2, respectively. In this case $P_1 = P_2 = 1 + \Gamma(\tau)\cos(\bar{\omega}\tau)$. For the case of the down-converted photons

$$C(\tau) \propto \int \int d\omega_1 d\omega_3 \Phi(\omega_1, \omega_3 - \omega_1)(1 + \cos(\omega_1\tau))(1 + \cos((\omega_3 - \omega_1)\tau)). \quad (3.12)$$

Then, we make use of the approximation given in Eq. (3.9) to obtain the final result

$$C(\tau)/C_0 = 1 + \frac{1}{2}\Gamma_P(\tau)\Gamma_F(2\tau) + (\Gamma_P(\tau) + 1)\Gamma_F(\tau)\cos(\bar{\omega}_F\tau) + \frac{1}{2}\Gamma_P(\tau)\cos(2\bar{\omega}_F\tau), \quad (3.13)$$

where $\Gamma_P(\tau) = \int d\omega_3 P(\omega_3 + \omega_P)\cos(\omega_3\tau)$ and $\Gamma_F(\tau) = \int d\omega_1 F(\omega_1 + \bar{\omega}_F)\cos(\omega_1\tau)$.

The coincidences interferogram in Eq. (3.13) features four contributions. The DC term C_0 is given by the average number of coincidences. The second term corresponds to the interference of two monochromatic modes. This term is equivalent to the HOM dip explained in section 2.4.2. The third term accounts for the interference of two photons going through different arms (cases *iii* and *iv* in Fig. 3.1b). The last term originates from the interference of both photons traveling along the same path (cases *i* and *ii* in Fig. 3.1b).

Let us now to illustrate Eq. (3.13) by considering three different cases:

Completely entangled state This case corresponds when $\gamma \rightarrow \infty$ or equivalent when the coherence length L_F of the down-converted photons is $L_F \ll L_P$, where L_P is the coherence length of the pump [Fig. 3.4a].

Partially entangle state This is the intermediate case when $L_F \sim L_P$ and is a superposition of a completely entangled state and a separable state [Fig. 3.4b].

Separable state In this case $\gamma \rightarrow 0$ which happens when $L_F \gg L_P$ [Fig. 3.4c].

3.1 Experimental Results

To experimentally confirm Eq.(3.13), we measured the fourth-order interferogram with two different pairs of filters. Our experiments used a 100 mW diode laser with nominal wavelength of 407 nm and coherence length of 200 μm. The laser pumps a BBO nonlinear crystal whose optical axis is oriented at 3.6 degrees with respect to the propagation direction of the laser (refer to appendix A). This configuration produces Type I collinearly propagating down-converted photons pairs with degenerate center wavelengths of 814 nm [37]. After the crystal, the pump laser is suppressed with a combination of a polarizing beam splitter and a longpass filter. The down-converted photons are sent into a Michelson interferometer and the output is analyzed by means of coincidence detection (Fig. 3.5).

We adjust the path-length difference between the interferometer arms to zero by using a white-light source with a coherence length of 50 μm. The path-length of one of the interferometer arms can be adjusted by translating the end mirror with a piezo motor. The latter
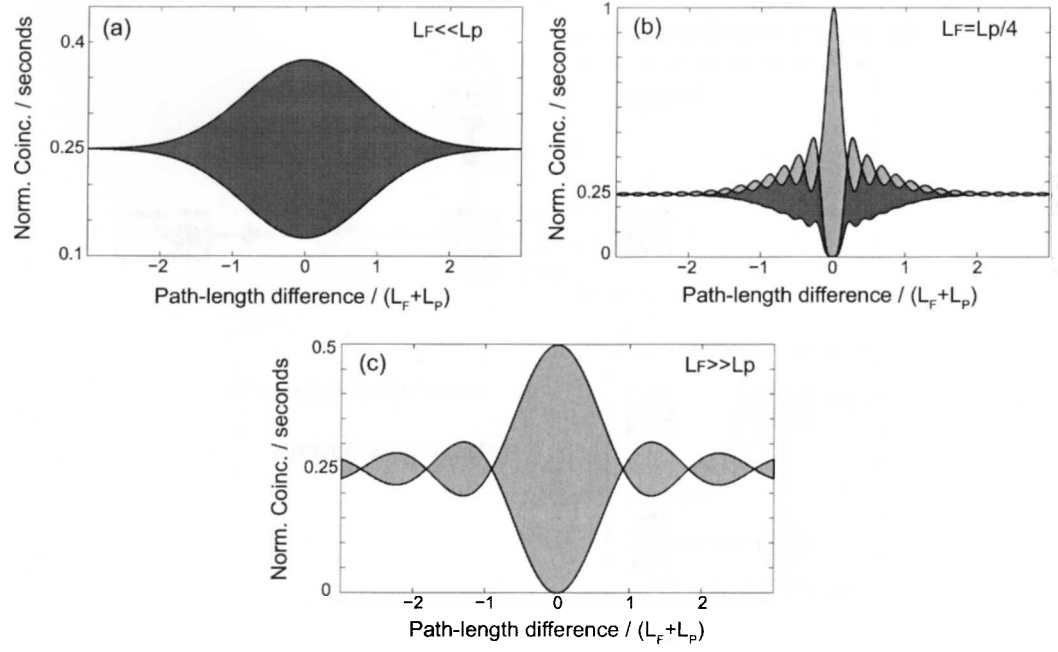
Figure 3.4: Examples of interference patterns for three different cases. The gray shade indicates fringes with frequency ω_F and the darker shade fringes with frequency $2\omega_F$. (a) The coherence length L_F of the down-converted photons is much smaller than the coherence length L_P of the pump. In this case the down-converted photons are completely entangled. (b) In the intermediate case when $L_F \sim L_P$ the interference pattern is a superposition of a complete entangle state and a separable state. (c) The state becomes separable when $L_F >> L_P$.

has a step size of 20 nm. In the experiment, we synchronize the translation of the mirror with the acquisition of photon coincidences. Our coincidence counting procedure has a time-bin resolution of 4 ps. An electronic delay of 100 ns has been introduced in one of the detection channels in order to shift the central position of the coincidences peak. For all measurements we used an acquisition time of $T = 10$ seconds and counted all coincidences in a time window $\tau = 3$ ns. Background counts were subtracted using the relation $AB\tau/T$, where A and B are the single photon counts of detector A and B, and τ and T are the time window and the acquisition time, respectively.

In our theoretical calculations we assumed that the spectrum of the pump laser is Gaussian with a central wavelength of 407 nm and a FWHM of 0.36 nm, which produces a coherence length $L_P \sim 200$ μm, in agreement with the specifications of the laser. The bandwidth of the down-converted photons is limited by bandpass filters that are placed in front of the detectors. For the first experiment, the filters have a bandwidth of 10 nm centered at 810 nm (the center wavelength is not exactly at the degenerate wavelength of 814nm, however, because $\Delta\omega_F > \Delta\omega_P$ we can still assume that the phase matching function $H \approx 1$ in the region defined by the filters). For the second experiment, we use bandpass filters with bandwidths of about 200 nm. In this case, the factor γ and the degree of entanglement increase, which is
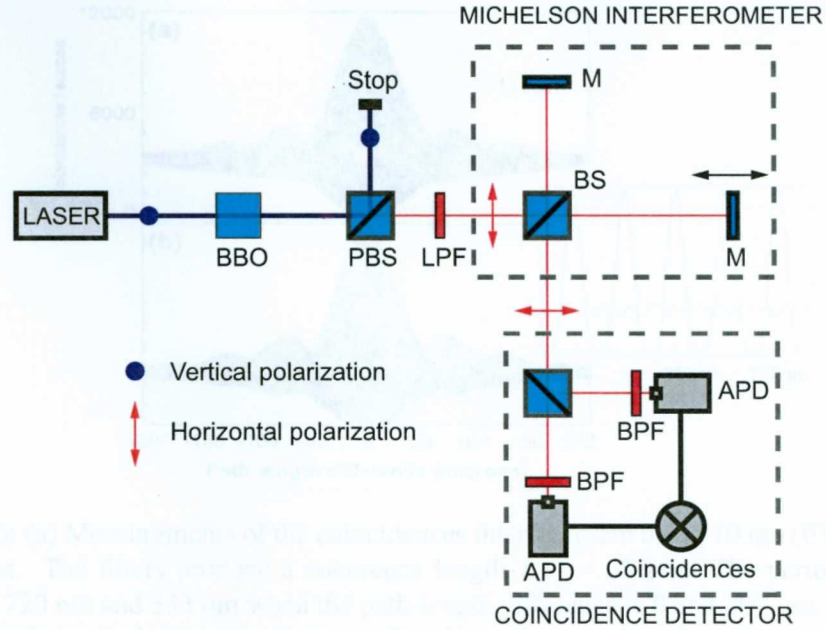
Figure 3.5: Schematic of the experiment. BBO: β-barium borate crystal, PBS: polarizing beam splitter, LPF: long pass filters, BS: beam splitter, M: mirror, APD: avalanche photodiode, BPF: band pass filters.

clearly noticeable in the interferogram.

Fig. 3.6a shows the measurements of the fourth-order interferogram using the 10 nm filters. The frequency bandwidth selected by the filters gives rise to a coherence length of $L_F = 55$ μm. The inset shows a close-up of the fringes in two different regions. In the center region the oscillations feature a wavelength of 720 nm (visibility of 0.99). On the other hand, for a path-length difference of 200 μm, the period reduces to 333 nm (visibility of 0.11). The corresponding theoretical calculations based on Eq. (3.13) are shown in Fig. 3.6b. The theory yields an oscillation frequency of $\overline{\omega}_F$ for short path-length differences and $2\overline{\omega}_F$ for path-length differences larger than the coherence length. Slight differences between theory and experiment are due to the hysteresis and finite step size of the piezo motor used for mirror translation (the average step size is 20nm, which generates a path-length difference of 40nm for each step). Nevertheless, there is good agreement between theory and the experiment.

Fig. 3.7a shows the experimental fourth-order interferogram using bandpass filters with a 200 nm bandwidth. The filters produce a coherence length of roughly $L_F = 3.3\mu m$. In the center region, the fringes have a period of 563 nm and a visibility of 0.99. When the path-length difference becomes equal to 60 μm, the wavelength reduces to 141 nm and the visibility reduces to 0.19. The theoretical calculations are shown in Fig. 3.7b. The slight frequency mismatch is again due to the precision of the piezo motor. Also, background noise from the pump laser slightly reduces the visibility of the experimentally recorded fringes. Overall, there is good agreement between theory and experiment. Clearly, the degree of entanglement
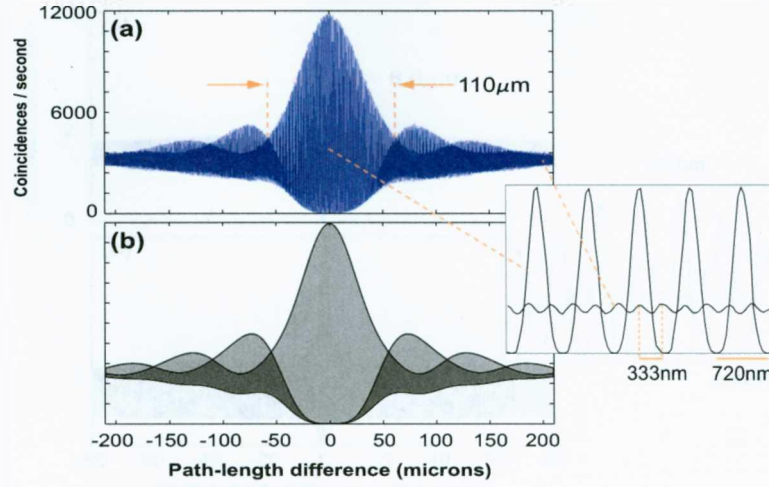
Figure 3.6: (a) Measurements of the coincidences interferogram using 10 nm (FWHM) band-pass filters. The filters produce a coherence length $L_F = 55$ μm. The periodicity of the fringes is 720 nm and 333 nm when the path-length difference is 0 and 200 μm, respectively. The theoretical calculations are shown in (b). The coherence length of the pump photons is $L_P = 200$ μm.

in this experiment is stronger than in the previous one. Since the frequency bandwidth of the filters is increased, the value of γ increases compared to the first experiment (remember that the frequency bandwidth $\Delta\omega_F \propto \Delta\lambda_F$ where $\Delta\lambda_F$ is the wavelength bandwidth). In other words, the area of the joint spectral density selected with the 200 nm bandpass filters is more asymmetric (c.f. Fig. 3.2) than the joint spectral density recorded with 10 nm bandpass filters.

3.1.1 Conclusions

We have analyzed the two-photon Michelson interferometer with entangled down-converted photons. The fourth-order interferogram is given in terms of the pump spectral density and bandwidth of the bandpass filters [Eq. (3.13)]. We showed that the degree of entanglement increases with the ratio $\gamma = \Delta\omega_F/\Delta\omega_P$, where $\Delta\omega_P$ and $\Delta\omega_F$ are the spectral bandwidths of the pump laser and bandpass filters, respectively.

We emphasize that γ is not a parameter that can be used to discard hidden variables theories as such as the Bell's inequality. However, it can be used to compare the degree of entanglement between different experiments. Another important comment, the Michelson interferometer cannot be used for proving nonlocal behavior or for measuring a Bell-type inequality. The reason is that the two photons have the same propagation mode and therefore, if we apply a projection, both photons are affected simultaneously. In order to measure a Bell-type inequality, both photons should be emitted in different directions and each of them introduced in an interferometer [38]. Furthermore, in our analysis we consider that all the four scenarios shown in Fig. 3.1b are measured in the coincidences. We can adjust the time window of the coincidences detector in order to discard the cases when signal and idler photons travel
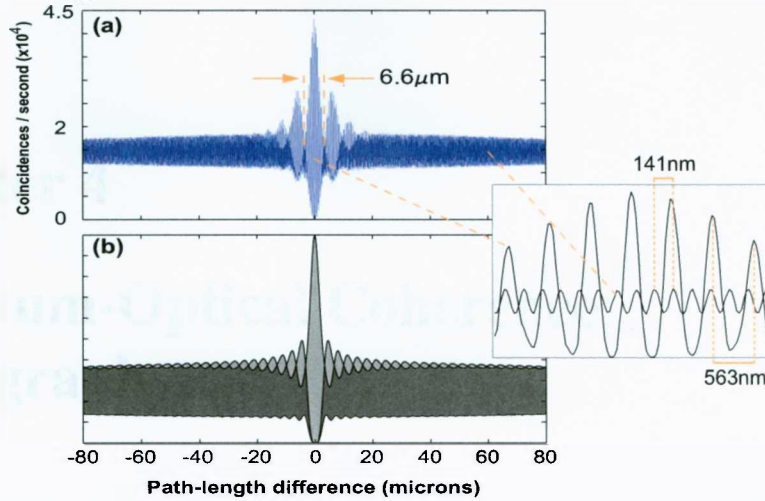
Figure 3.7: (a) Measurements of the coincidences interferogram using 200 nm bandpass filters which produces a coherence length of 3.3 μm. The measurements are shown in (a) and theoretical calculations in (b). Compared to the first experiment, the degree of entanglement in the second experiment is higher.

through different directions (cases *iii* and *iv* in Fig. 3.1). By doing this, the interferogram only include the superposition of the cases *i* and *ii* when both photons travel together which produces an interference pattern similar to the example in Fig. 3.4a but with better visibility [39]. Appendix A shows an experiment where we increase the path-length difference in order to distinguish the different pathways of the down-converted photons.

We experimentally measured the complete fourth-order interferogram and the results agree with the theoretical predictions. The next chapter shows how to use the two-photon Michelson interferometer for QOCT. As we will show, the second term or bunching term in Eq. (3.13) is identical to the results obtained with the standard configuration of QOCT using a HOM interferometer [6, 7], that is, dispersion cancelation and enhancement of resolution by a factor of two. Clearly, from Eq. (3.13) the bunching term is spectrally separated from the other contributions and hence, we can filter out the other elements by Fourier processing the coincidences interferogram.

Chapter 4

Quantum-Optical Coherence Tomography

This chapter studies the implementation of QOCT using the two-photon Michelson interferometer with down-converted photons. We start introducing the mathematical description of the classical OCT and the standard QOCT with the HOM interferometer. Then, we introduce the theory of QOCT using the two-photon Michelson interferometer and discuss its advantages and limitations with numerical simulations. Then, we show the results of our proof of principle experiments.

4.1 Comparison of OCT and QOCT

Let us start with a brief discussion of the principles underlying OCT. The basic configuration of OCT is shown in Fig. 4.1a. OCT makes use of a classical light source with a short coherence time and implements a standard Michelson interferometer to measure the interference pattern of the reflected light from a sample located in one of the interferometer arms. The reflection from the sample is represented by a transfer function $s(\omega)$ which contains all the information regarding the internal layers. For an incident monochromatic plane wave with angular frequency ω,

$$s(\omega) = \int_0^\infty r(z, \omega) e^{i2\varphi(z, \omega)} \mathrm{d}z, \tag{4.1}$$

where $r(z, \omega)$ is the complex reflection coefficient from a layer at position z and $\varphi(z, \omega)$ is the phase accumulated by the wave while traveling through the sample to the depth z. We assume that the medium is homogeneous, isotropic and there is not absorption.

The source is characterized by a power spectral density $P(\omega_p + \Omega)$, where Ω is the angular frequency deviation about the central frequency ω_p. The source has a bandwidth $\Delta\omega_p$ at FWHM. For simplicity, we assume that P is a symmetric function. The reference arm introduces a variable delay time τ while the sample is located at the second arm. The intensity I at the output of the interferometer is measured using a photodetector. The delay τ is swept and the interference pattern or interferogram $I(\tau)$ is recorded. Considering a sample with a transfer function given by Eq. (4.1), the interferogram becomes proportional to

$$I(\tau) \propto \Gamma_0 + 2\mathrm{Re}\{\Gamma(\tau)\} \cos(\omega_p \tau), \tag{4.2}$$

33

where the average intensity Γ_0 and the interference term $\Gamma(\tau)$ are given by

$$\Gamma_0 \;=\; \int d\Omega \left[1 + |s(\omega_p + \Omega)|^2\right] P(\Omega), \tag{4.3}$$

$$\Gamma(\tau) \;=\; \int d\Omega\, s(\omega_p + \Omega) P(\Omega) e^{-i\Omega\tau}. \tag{4.4}$$

Notice that Eq. (4.2) is equivalent to Eq. 2.23 when the sample is replaced by a mirror. The average intensity Γ_0 includes a factor of unity given by the self-interference of the light reflected from the reference arm and a factor $|s(\omega_p + \Omega)|^2$ from the sample path. The cross-interference term comes from the product of both contributions. This term can also be expressed as the convolution of the sample reflection with the temporal coherence function of the source which defines the resolution of OCT.
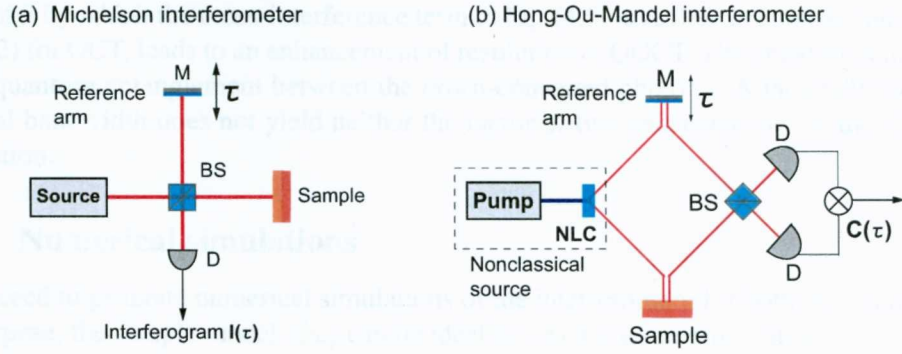

Figure 4.1: (a) Implementation of Optical Coherence Tomograhpy. (b) Implementation of Quantum-Optical Coherence Tomography using a Hong-Ou-Mandel interferometer.

We now turn to the case of QOCT, which is illustrated in Fig. 4.1b. QOCT implements a HOM interferometer with a source of non-collinear entangled photons. The entangled photons are generated by spontaneous parametric down-conversion. We assume that the nonlinear crystal is pumped by a monochromatic laser with angular frequency ω_p and that the joint probability amplitude $\phi(\omega_1, \omega_2)$ of the down-converted photons is symmetric with respect to the central frequency $\omega_0 = \omega_p/2$. Therefore, ϕ can be expressed as function of the frequency deviation Ω about the central frequency ω_0, i.e. $\phi(\omega_1, \omega_2) \rightarrow \phi(\Omega)$. The spectral density $\Phi(\Omega) = |\phi(\Omega)|^2$ is normalized such that $\int d\Omega \Phi(\Omega) = 1$. For simplicity, both photons have the same polarization and spatial mode, which corresponds to SPDC of type I. The initial state of the down-converted photons is written as

$$|\psi\rangle = \int d\Omega\, \phi(\Omega) |\omega_0 + \Omega\rangle |\omega_0 - \Omega\rangle. \tag{4.5}$$

The HOM interferometer is modified by placing the sample in one of the interferometer arms. The delay τ is swept and the coincidences $C(\tau)$ are monitored. The coincidences of photons arriving at the two detectors are recorded within a time window determined by the

coincidences circuit. For a sample described by $s(\omega)$, as provided in Eq. 4.1, the coincidences rate $C(\tau)$ is proportional to

$$C(\tau) \propto \Lambda_0 - \mathrm{Re}\{\Lambda(2\tau)\}, \tag{4.6}$$

where the self-interference term Λ_0 and the cross-interference term $\Lambda(\tau)$ are

$$\Lambda_0 = \int d\Omega |s(\omega_0 + \Omega)|^2 \Phi(\Omega), \tag{4.7}$$

$$\Lambda(\tau) = \int d\Omega s(\omega_0 + \Omega) s^*(\omega_0 - \Omega) \Phi(\Omega) e^{-i\Omega\tau}. \tag{4.8}$$

Notice that the unity background factor present in Eq. (4.3) for OCT is absent in Λ_0, which favors the signal to noise ratio (SNR). Moreover, the QOCT cross-interference term $\Lambda(\tau)$ probes the sample at two frequencies, $\omega_p + \Omega$ and $\omega_p - \Omega$, in a multiplicative fashion. In addition, as we will see, $\Lambda(\tau)$ generates terms that are independent of the sample dispersion. Finally, the factor of 2 by which the cross-interference term in Eq. (4.6) is scaled, in comparison to that in Eq. (4.2) for OCT, leads to an enhancement of resolution in QOCT. The enhancement is result of the quantum entanglement between the down-converted photons. A factorable state with identical bandwidth does not yield neither the factor of two enhancement nor the dispersion cancelation.

4.1.1 Numerical simulations

We proceed to generate numerical simulations of the interferogram for both applications. For that purpose, the sample model $s(\omega)$ can be idealized as a discrete summation

$$s(\omega) = \sum_j r_j(\omega) e^{j2\varphi_j(\omega)}, \tag{4.9}$$

where the summation index extends over the layers that constitute the sample. This is a customary approximation for many biological samples that are naturally layered, as well as for other samples that are artificially layered such as semiconductor devices. For simplicity, we assume that the dispersion profile of the medium between all layers is identical, so that $\varphi_j(\omega) = \beta(\omega)z_j$, where $\beta(\omega) = n(\omega)\omega/c$ is the wave number at angular frequency ω, z_j is the depth of the jth layer from the sample surface ($z_0 = 0$), $n(\omega)$ is the frequency dependent refractive index and c is the speed of light in vacuum. Expanding $\beta(\omega_0 + \Omega)$ to second order in Ω

$$\beta(\omega_0 + \Omega) \approx \beta_0 + \beta_0'\Omega + \frac{1}{2}\beta_0''\Omega^2, \tag{4.10}$$

where $\beta_0' = \beta'(\omega_0)$ is the inverse of the group velocity $v_0 = 1/\beta'(\omega_0)$, and $\beta_0'' = \beta''(\omega_0)$ represents the group velocity dispersion (GVD). The cross-interference term in OCT [Eq.(4.4)] can be written as

$$\Gamma(\tau) = \sum_j r_j \zeta_d^{(0j)} \left(\tau - 2\frac{z_j}{v_0}\right) e^{i2\beta_0 z_j}, \tag{4.11}$$

where $\zeta_d^{(0j)}$ comes from reflection from the jth layer after suffering GVD over a distance $2z_j$, the subscript d indicates dispersion and the superscript $(0j)$ indicates that the dispersion

is included from the initial surface of the sample to the jth layer. The quantity $\zeta_d^{(jk)}$ is the Fresnel transformation of $P(\Omega)$ with dispersion coefficient β_0'' [14]

$$\zeta_d^{(jk)}(\tau) = \int d\Omega P(\Omega) e^{i2\beta_0''\Omega^2(z_j - z_k)} e^{-i\Omega\tau}. \tag{4.12}$$

The resolution of OCT is therefore limited to samples with negligible GVD over the depth of interest.

For the case of QOCT, the discrete version of the cross-interference term $\Lambda(\tau)$ is given by the sum of two contributions

$$
\begin{aligned}
\Lambda(\tau) &= \sum_j |r_j|^2 \widetilde{\Phi}\left(\tau - 4\frac{z_j}{v_0}\right) \\
&+ \sum_{j \neq k} r_j r_k^* \zeta_d^{(jk)}\left(\tau - 2\frac{z_j + z_k}{v_0}\right) e^{i2\beta_0(z_j - z_k)},
\end{aligned} \tag{4.13}
$$

with $\widetilde{\Phi}(\tau)$ being the inverse Fourier transform of $\Phi(\Omega)$. Notice that the first contribution represents reflection from each layer without GVD. This term provides the information of the depth and reflectance of the layers that constitute the sample. The second contribution represents cross terms coming from interference between reflections from each pair of layers. These cross terms are dispersed due to propagation through the inter-layer distances $z_j - z_k$, and they carrier information about the sample dispersion that is not accessible via OCT.

Let us now show numerical comparison between OCT and QOCT. We consider two cases in order to emphasize the main differences, which are resolution enhancement and dispersion cancelation. In the first example the sample is a glass slab with refractive index $n = 1.6$. We neglect the dispersion of the glass. The aim is to show the resolution enhancement in QOCT. In the second example, the glass slab is buried at some depth in a highly dispersive medium. In this case the goal is to prove the dispersion cancelation in QOCT. For the purposes of our calculations, we choose amplitude reflection coefficients $r_1=0.5$ and $r_2 = 0.7$ and thickness $d = 150$ μm. For both OCT and QOCT we assume that the source has a central wavelength $\lambda_0 = 2\pi c/\omega_0 = 814$ nm and a Gaussian spectral distribution with a bandwidth of 10 nm which corresponds to a coherence length of about 55 μm. For QOCT this can be realized using a β-barium borate crystal pumped by a source with central wavelength of 407 nm. For the second example, the slab is at $d_1 = 2$ mm below the dispersive medium and we assume that the dispersion profile of the surrounded medium is characterized by $\beta' = 5 \times 10^{-9}$ s/m ($v_0 = 1/\beta' = 2 \times 10^8$ m/s) and $\beta'' = 88 \times 10^{-25}$ s^2/m. The reason to simulate this particular case, is because in ophthalmologic imaging, for example, the structure of interest is located behind a large body of dispersive ocular media.

Figures 4.2a and 4.2c show the result of the first example. As expected, the QOCT resolution is a factor of two superior to that achievable in OCT. The peak between the two dips is a result of quantum interference between the probability amplitudes arising from reflection from the two different surfaces. The dips are result of quantum interference between the probability amplitudes arising from reflection from each layer independently. The width of the middle peak is determined by the dispersion of the medium between the two surfaces and not by the surrounded medium. Therefore, the dispersion of the region between the two

surfaces may be determined by measuring the broadening of the middle peak in comparison with the two dips.

Figures 4.2b and 4.2d show the calculations of the second example. Because of dispersion, the coherence length for the OCT interferogram increases. On the other hand, QOCT remains unaffected and yields dispersion-canceled dips at locations corresponding to reflection from the two surfaces. The dispersion cancelation occurs for all even powers of the expansion of $\beta(\omega)$.
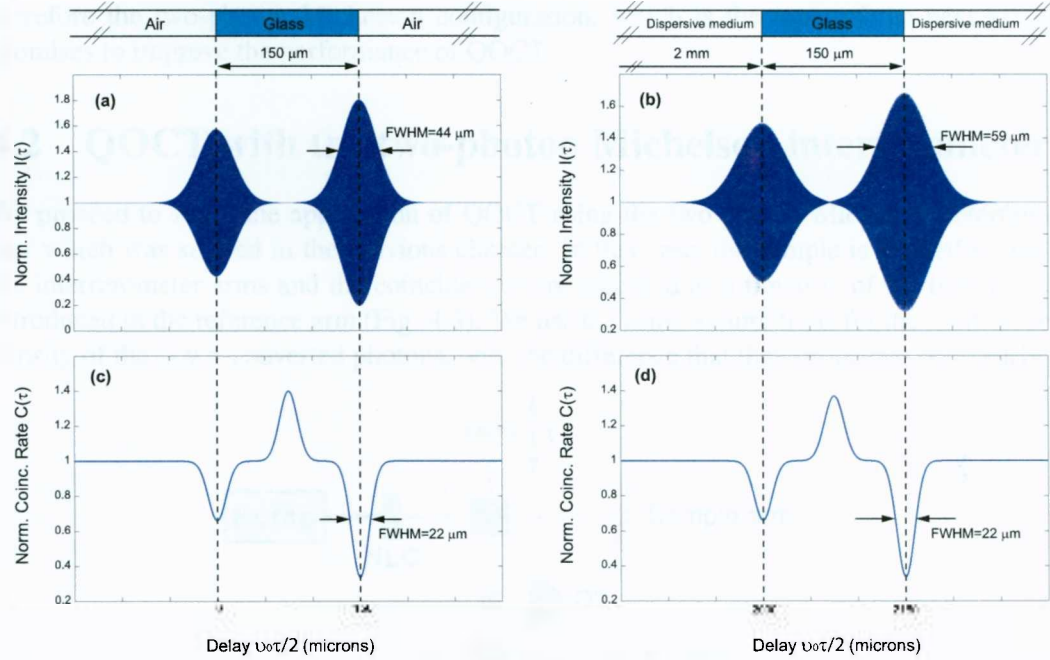

Figure 4.2: (a),(b) Numerical simulation of the intensity I(τ) versus the delay (scaled by half the group velocity $v_0/2$) for a two-layer sample for OCT. In (b) the sample is buried at 2 mm below the surface of a dispersive material. (c), (d) Coincidences rate $C(\tau)$ for QOCT using the same sample conditions. Notice the enhancement in resolution by a factor of 2 and the dispersion cancelation because of the entanglement between signal and idler photons.

In order to recover the useful information from the QOCT interferogram, we can average $\Lambda(\tau)$ with respect to the central frequency ω_0 such that the exponential function in the second contribution average to zero [refer to Eq. (4.13)]. The terms from the first contribution are not affected by the average and hence the information concerning the position and reflectance of the internal layers is obtained.

In summary the advantages of QOCT in comparison with OCT are:

1. greater signal to noise ratio, refer to Eq. (4.7),

2. resolution enhancement by a factor of two for the same source bandwidth, refer to Eq. (4.6),

3. interference terms that are insensitive to even-order dispersion of the medium, refer to Eq. (4.13)

4. interference terms that are sensitive to dispersion of the medium, providing information of the dispersive properties of the medium, Eq. (4.13).

It should be pointed out that the current sources of down-converted photons are weak so that the experiments require long integration times for reliable detection. We emphasize that high efficiency sources of down-converted photons operate in a collinear fashion, and therefore the two-photon Michelson configuration, which is the topic of the next section, promises to improve the performance of QOCT.

4.2   QOCT with the two-photon Michelson interferometer

We proceed to study the application of QOCT using the two-photon Michelson interferometer which was studied in the previous chapter. In this case, the sample is located in one of the interferometer arms and the coincidences are recorded as a function of the time delay τ introduced in the reference arm (Fig. 4.3). We use the same assumptions for the joint spectral density of the down-converted photons, with the difference that they propagate collinearly.
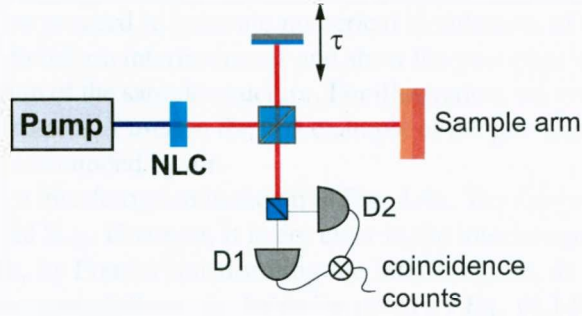

Figure 4.3: Quantum-Optical Coherence Tomography with the two-photon Michelson interferometer.

The resulting coincidences interferogram is a generalization of Eq. (3.13), which is given by the superposition of four contributions

$$C(\tau) \propto M_0 + 2\text{Re}\{M_1(2\tau)\} + 4\text{Re}\{M_2(\tau)\}\cos(\omega_0\tau) + 2\text{Re}\{M_3\}\cos(2\omega_0\tau), \quad (4.14)$$

with

$$M_0 = \int d\Omega\Phi(\Omega)(1 + |s(\omega_0 - \Omega)|^2)(1 + |s(\omega_0 + \Omega)|^2), \quad (4.15)$$

$$M_1(\tau) = \int d\Omega\Phi(\Omega)s(\omega_0 + \Omega)s^*(\omega_0 - \Omega)e^{-i\Omega\tau}, \quad (4.16)$$

$$M_2(\tau) = \int d\Omega\Phi(\Omega)s(\omega_0 + \Omega)(1 + |s(\omega_0 - \Omega)|^2)e^{-i\Omega\tau}, \quad (4.17)$$

$$M_3 = \int d\Omega\Phi(\Omega)s(\omega_0 + \Omega)s(\omega_0 - \Omega). \quad (4.18)$$

This interferogram is more complicated than the HOM interferogram. The four contributions come from the different pathways that the photon pairs can take through the interferometer (refer to Fig. 3.1). The self-interference term M_0 is the average number of coincidences. From its definition is equivalent to Γ_0 for the case of OCT [Eq. (4.3)]. The second contribution M_1, (which we call the bunching term in the previous chapter) is actually equal to the cross-interference term $\Lambda(\tau)$ for the case of QOCT with the HOM interferogram [Eq. (4.8)]. M_2 is produced by the cases when the signal and idler photons travel separately through the interferometer. Since each photon has central frequency ω_0 the fringes coming from the interference of these cases oscillate with frequency ω_0. The last contribution M_3 is produced by the cases when both photons travel together through the interferometer. In this case the bunch of the two photons result in fringe oscillations with twice the frequency of a single photon $2\omega_0$ (which is equal to the pump frequency).

This interferogram by itself doesn't provide more information than the interferogram given by the single photon Michelson interferometer in the classical OCT. On the contrary, the interference pattern results more complicated to analyze because the fringes oscillate at two frequencies ω_0 and $2\omega_0$. This could be the reason that this interferometer had not been applied in QOCT. However, as we can see from Eq. (4.14), the contribution given by M_1 is frequency isolated from the other terms and therefore we can Fourier process the interferogram to filter out this term. As we mentioned, $M_1(\tau)$ is equal to the cross-interference term $\Lambda(\tau)$ in the HOM interferogram and therefore it contains all the properties that we emphasized previously. With this in mind, we proceed to generate numerical simulations of the interferogram given by the two-photon Michelson interferometer and show the post-processing process in order to recover the information of the sample structure. For illustration, we generate the interferogram taking the same parameters as used in the first example of the previous cases. So, we consider a 150 μm glass slab surrounded by air.

The coincidence interferogram is shown in Fig. 4.4a. The fringes oscillate at two different frequencies ω_0 and $2\omega_0$. However, it is not clear in the interferogram because of the scale of the abscissas. But, by Fourier transforming the interferogram, as show in Fig. 4.4b, it is clear that the interferogram follows the behavior given by Eq. (4.14). The solid line in Fig. 4.4a is the term $2\mathrm{Re}\{M_1(2\tau)\}$. It is clear that this term is equivalent to the term $-\mathrm{Re}\{\Lambda(2\tau)\}$ in QOCT [Eq. (4.6)], which contains the location of the layers and information regarding the inter-layers dispersion. In Fig. 4.4b we have subtracted the average coincidences. In order to obtain the term $2\mathrm{Re}\{M_1(2\tau)\}$ we implement a low-pass filter center at the zero frequency. The bandwidth $\Delta\omega_f$ is larger than the bandwidth of $M_1(\omega)$. The frequency bandwidth of $M_1(2\tau)$ is twice the bandwidth $\Delta\omega$ of the joint spectral density $\Phi(\Omega)$. Therefore, the bandwidth of the numerical filter should be minimum $2\Delta\omega$ but not large enough to take frequency components from the other terms.

Let us now discuss the procedure to extract the location of the layers from the coincidences interferogram. As we can see from Eq. (4.13), the second term which contains the inter-layers information oscillates with respect to $\beta_0 = n(\omega_0)\omega_0/c$. After filtering the interferogram, in order to obtain the location of the layers, we can average over the central frequency ω_0 until the second term vanishes. For illustration, we show in Fig. 4.5 the behavior of the interferogram when we change the central frequency. Clearly, the location of the layers is unaffected by the averaging process. As expected, the central peak oscillates with respect to β_0.
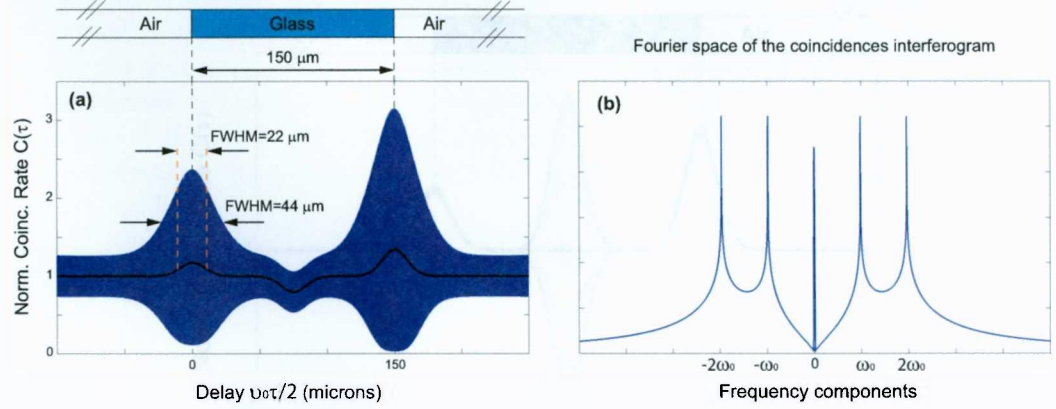
Figure 4.4: (a) Numerical simulations of the coincidences rate for the two-photon Michelson interferometer. (b) Fourier transform of the coincidences interferogram showing the elements in Eq. (4.14). The black solid line in (a) results from filtering the zero frequency component in (b).

We can implement this property for studying turbulent media. Since the positions of the layers are unaffected by varying β_0, we can trace the interferogram of a turbulent medium in several occasions and only the middle peaks will disappeared after averaging the interferograms. This is a research topic to be developed eventually.

4.2.1 Proof-of-principles experiments

We now show our proof-of-principles experiments to demonstrate the previous ideas. We perform two experiments, in the first one we use the same configuration as shown in Fig. 3.5. We measured the interference pattern using a mirror in the sample arm. The goal of this experiment is to show the post-processing process. We used 10 nm bandpass filters in front of each detector, and since the bandwidth of the filters is smaller than the bandwidth of the down-converted photons, we can approximate the function $\Phi(\Omega)$ by the transmissivity $F(\Omega)$ of the filters, as explained in the previously. The resulting coincidences interferogram with the filtering process is shown in Fig. 4.6. We can see that the solid line shows a $sinc$ behavior, which is result of the uniform distribution of the bandpass filters. Remember that in Eq.(4.13) the first term contains the inverse Fourier transform of the spectral density, which in this case the inverse Fourier transform of the uniform distribution is equal to a $sinc$ function. Fig. 4.6b shows the Fourier transform of the interferogram where we have subtracted the average coincidences. In order to obtain the bunching term we filter the spectral content at the zero frequency. Notice that resulting filtered interferogram in Fig. 4.6a contains the resolution enhancement as expected.

In a second experiment, we used as a sample a glass cover slip with a thickness of about 100 microns. In order to increase the reflectivity of the surfaces, we deposited on each of them a 10 nm gold layer. The resulting interferogram is shown in Fig. 4.7 together with the interferogram after the filtering process. The filtered interferogram is shown after subtracting
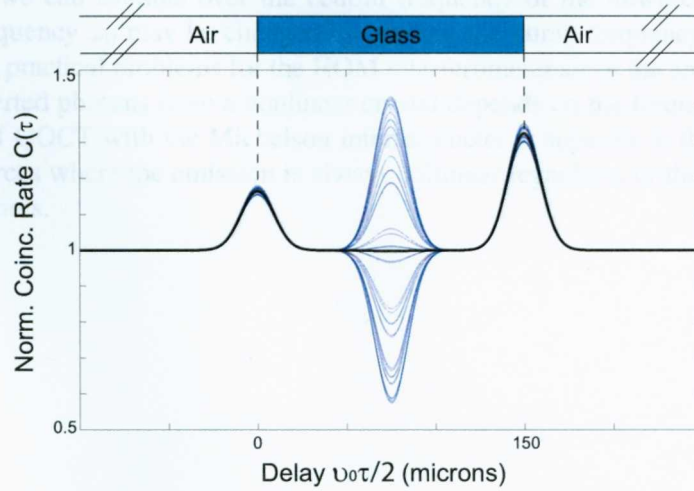
Figure 4.5: Recovering the location of the layers. The peaks indicating the position of the layers in the coincidences interferogram are unaffected by changing the propagation constant $\beta_0 = n(\omega_0)\omega_0/c$. The solid line shows the average after varying the β_0. The central peak oscillates with respect to β_0 whereas the layer positions remain constant.

the average coincidences rate and taking the absolute value. The important things to notice are the reduced coherence length and the peak between the surfaces. As we explained before, the central peak comes from the superposition of the reflections from both surfaces. The width of this peak is sensitive to the dispersion of the medium and can be subtracted by averaging over ω_0. The side peaks are due to the *sinc* functions imposed by the bandpass filters. The side peaks become a problem for locating the peaks that correspond to the location of the layers. We can use filters with a Gaussian transmissivity in order to eliminate this side peaks. The filtered interferogram clearly shows the expected behavior.

4.2.2 Conclusions

We have presented the conditions for applying the two-photon Michelson interferogram for QOCT. We derived the resulting coincidences interferogram [Eq. 4.14] and shown that the interferogram can be Fourier processed in order to obtain the same information as the HOM interferometer. In comparison with the HOM interferometer, the Michelson interferometer offers practical advantages such as robustness and simplicity with the cost of numerical processing. However, the numerical processing is straightforward implemented using Fourier analysis. We shown that as long as the spectral bandwidth of the down-converted photons is smaller than their central frequency, the two-photon Michelson interferometer can be successfully used for QOCT. A disadvantage of our configuration is to filter out the pump laser after the nonlinear crystal. However, since the polarization of the pump photons is orthogonal to the polarization of the down-converted photons, we can use polarizing elements to eliminate the pump laser.

We mentioned that in order to recover the location of the layers from the coincidences

interferogram, we can average over the central frequency of the down-converted photons. The central frequency ω_0 may be changed by varying the pump frequency $\omega_p = 2\omega_0$. This technique faces practical problems for the HOM interferometer since the angle of emission of the down-converted photons from a nonlinear crystal depends on the frequency of the pump. Our proposal of QOCT with the Michelson interferometer is superior in this aspect because we can use sources where the emission is always collinear regardless of the pump frequency, e.g. photonic fibers.

(a) Coincidences interferogram
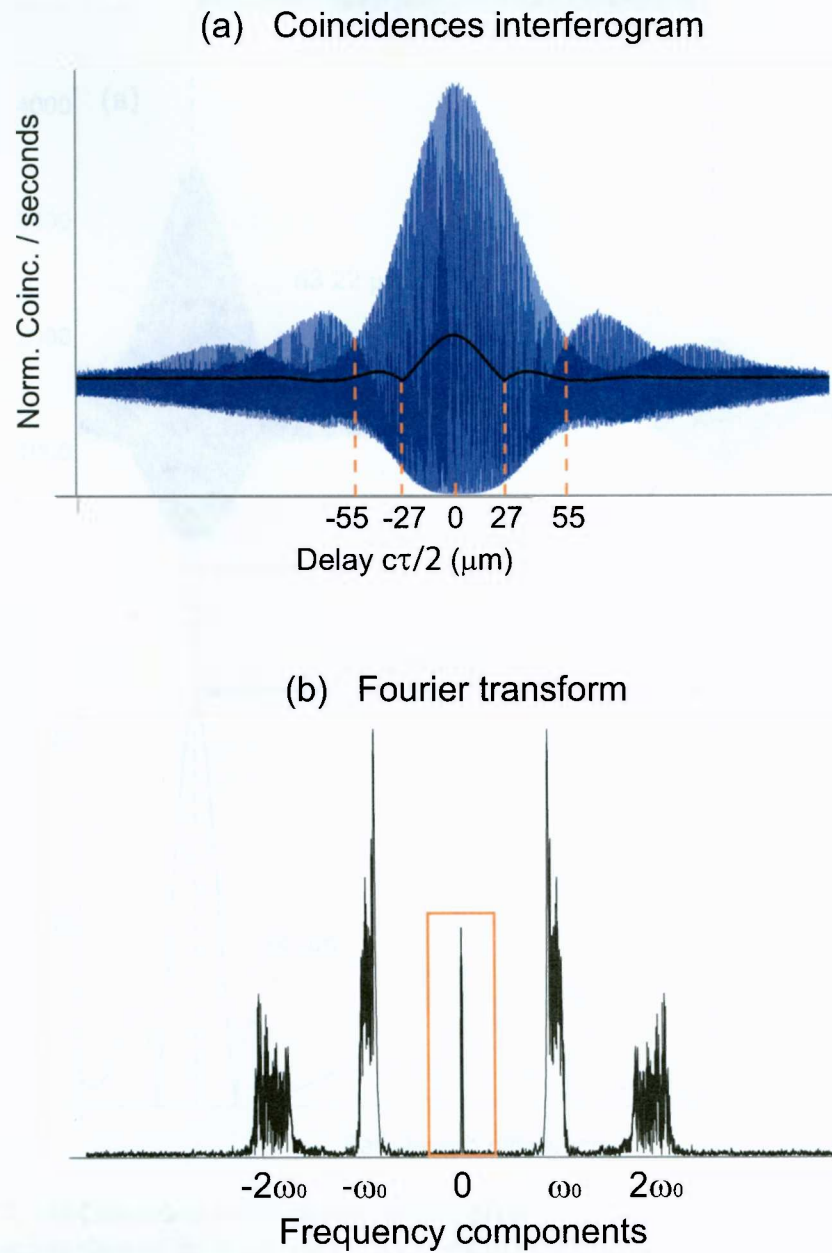

(b) Fourier transform

Figure 4.6: Proof of principle experiment. (a) Coincidences interferogram for single reflective layer. The black solid line results from filtering the zero frequency component from the Fourier space (b).
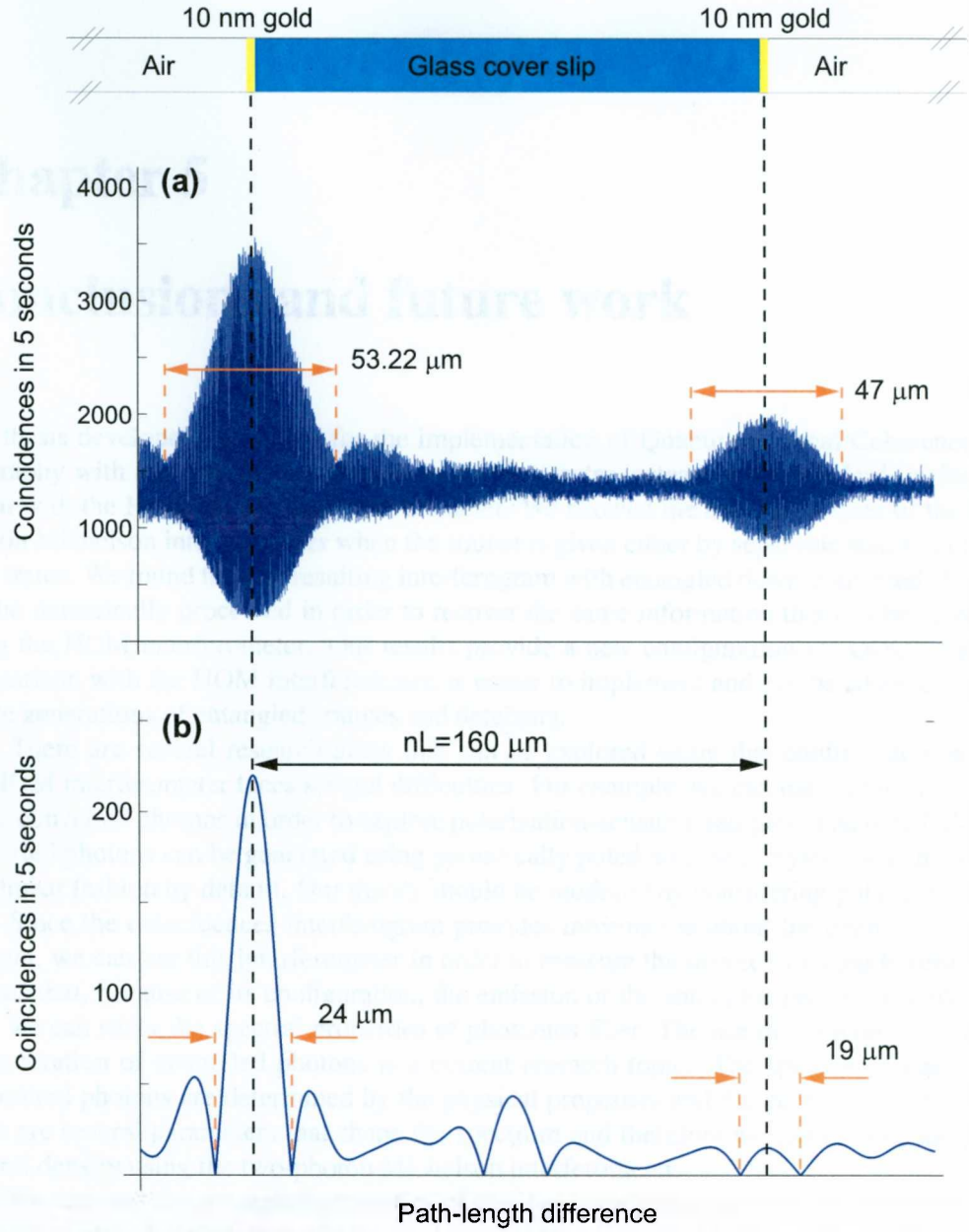
Figure 4.7: (a) Coincidences interferogram of a glass cover slip. We deposit a thin layer of gold on each surface of the glass cover slip i n order to increase the reflectivity of the surfaces. From the interferogram, we can observe that at the position of the layers the fringes oscillate at ω_0 and they oscillate at $2\omega_0$ at the middle of the sample. We used an piezo motor average step size of 22.6 nm (as explained in Appendix A), equivalent to a free-space thickness of 160 μm. If we consider a glass refractive index $n = 1.5$, the cover slip has a thickness of about 106 μm. (b) Filtered interferogram. We did the same procedure as in Fig. 4.6. We Fourier transform the interferogram and take the zero-frequency components. We show the result of the filtering process subtracting the average concidences rate and taking the absolute value. As expected, the filtered interferogram shows the position of the layers with a reduced coherence length. In addition, we can observe a central peak, coming from the interference of reflections on both surfaces.

Chapter 5

Conclusions and future work

The thesis developed the theory for the implementation of Quantum-Optical Coherence Tomography with the two-photon Michelson interferometer instead of the standard implementation with the Hong-Ou-Mandel interferometer. We showed the basic principles of the two-photon Michelson interferometer when the source is given either by separable states or entangled states. We found that the resulting interferogram with entangled down-converted photons can be numerically processed in order to recover the same information that can be achieved using the HOM interferometer. Our results provide a new configuration for QOCT that, in comparison with the HOM interferometer, is easier to implement and can be adapted for the future generations of entangled sources and detectors.

There are several research areas that can be explored using this configuration where the HOM interferometer faces several difficulties. For example, we can use collinear Type II down-converted photons in order to explore polarization-sensitive samples. The type II down-converted photons can be generated using periodically poled nonlinear crystals which emit in a collinear fashion by default. Our theory should be modified by considering polarization.

Since the coincidences interferogram provides information about the degree of entanglement, we can use this interferometer in order to measure the degree of entanglement with sources that, because of its configuration, the emission of the entangled photons is collinear, e. g. we can study the spectral properties of photonics fiber. The use of photonics fibers for the generation of entangled photons is a current research topic. The spectral properties of the emitted photons are determined by the physical properties and the geometry of the fiber. There are several parameters that shape the spectrum and therefore we can explore the joint spectral density using the two-photon Michelson interferometer.

We can use the entangled properties of the down-converted photons in order to study turbulent media. A turbulent media is characterized by a refractive index spectrum that varies from point to point. As we shown in Chapter 4, the coincidences interferogram is immune to sample dispersion and therefore we can recover the position of the internal layers of the sample by averaging several measurements.

Another interesting feature, is the oscillating peak that appears between two layers. The physics is similar to a standing wave, the length of which is determined by the separation of the adjacent layers. This behavior is not present in classical OCT. We could generate a physical model of the sample analogous to the standing wave and obtain the oscillation modes. This could provide an elegant method to recover the sample structure.
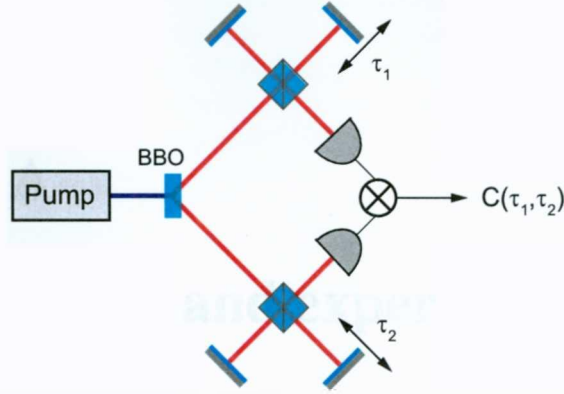
Figure 5.1: Experimental proposal. Each down-converted photon is sent into a Michelson interferometer. The coincidences interferogram $C(\tau_1, \tau_2)$ is a two-dimensional function depending on the delays τ_1 and τ_2 introduced by the interferometers. A Bell-type inequality can be calculated from $C(\tau_1, \tau_2)$.

Finally, we can extend our theory to develop a Bell inequality measurement for the non-collinear down-converted photons in the energy degree of freedom. Most of the Bell inequality measurements are done with the polarization degree of freedom. In order to measure the degree of entanglement using energy entangled photons, it is customary to implement a Franson experiment [38] where both signal and idler photons are sent into a Mach-Zehnder interferometer. Then, by means of post-selection (refer to Appendix A), they measure a type of Bell inequality and therefore the degree of entanglement. However, this is not the degree of entanglement coming from the source, this is now the degree of entanglement for a different quantum state that has been modified by the interferometers. I propose to implement a different experiment that doesn't require postselection and can be use to reconstruct the complete joint spectral density.

In order to understand the idea, notice that in the classical Michelson interferometer, the interferogram $I(\tau)$ contains in the interference term the information of the spectral density $\Phi(\omega)$, which can be reconstructed by processing the Fourier transform of $I(\tau)$. For the case of non-collinear down-converted photons, we can send each photon to a Michelson interferometer and measure the coincidences (Fig. 5.1). Each interferometer introduces a delay τ. The coincidences interferogram is then a function of both delays $C(\tau_1, \tau_2)$. We can trace the space τ_1, τ_2 and then by means of a two-dimensional Fourier transform we can recover the complete joint spectral density $\Phi(\omega_1, \omega_2)$. The collinear configuration is a special case when the two interferometers overlap and then $\tau_1 = \tau_2$. After obtaining $\Phi(\omega_1, \omega_2)$ we can measure the degree of entanglement using the Schmidt decomposition [24].

In conclusion, this thesis work demonstrates a novel and elegant procedure for realizing Quantum-Optical Coherence Tomography with the advantages of simplicity, performance and adaptability.

Appendix A

Instrumentation and experimental implementation

This appendix reviews the details for the experimental implementation.

A.1 Determination of the pump laser

The efficiency for generating down-converted photons is proportional to the nonlinear suscep-tibility $\chi^{(2)}$ which depends on the pump frequency. In addition, the maximum efficiency of the photodetectors that were used in our experiments is 80 % for 700 nm and drop off below 10 % for 1000 nm. The efficiency is important since the efficiency of the coincidence detection is the product of both photodetectors. Therefore, the choice of the laser pump is limited by the efficiency requirements.

It is customary to generate down-converted photons in the near infrared to operate de-tectors with high efficiency. To obtain near-infrared down-converted photons the best pump laser is a UV laser. In our experiments we use a 407 nm diode laser with produces 814 nm down-converted photons. At this wavelength the efficiency of the photodetectors is about 60 %. Therefore, the efficiency of a coincidence is 36 %.

A.2 Solving the phase-matching condition

We use a β-barium borate (BBO) nonlinear crystals cut for type-I parametric down-conversion to produce down-converted photons with linear polarizations parallel to each other but orthog-onal to the pump laser. The BBO crystal that was used in the experiments is cut at $30.4°$ with respect to the normal of the frontal face of the crystal. The polarization of the 407 nm pump laser is oriented for the extraordinary mode of the BBO crystal which emits down-converted photons forming a conical angle of $6°$. For the purpose of this thesis, however, we need to rotate the crystal in order to generate collinear down-converted. In order to calculate the angle of incidence, we need first to solve the phase-matching condition given in Eq. (2.10) for the collinear emission, which turns out to be

$$n_e(2\omega_0, \theta) = n_o(\omega_0),$$
(A.1)

where $\omega_0 = \omega_p/2$ is the angular frequency of the degenerate down-converted photons which is half the frequency of the pump photons. n_e and n_o are the extraordinary and ordinary refractive index of the crystal. The extraordinary refractive index depends on the angle θ between the propagation direction of the pump and the optics axis of the crystal. The refractive index n_e for a birefringent crystal is equal to

$$n_e(\omega, \theta) = \left[\frac{\cos^2(\theta)}{n_O^2(\omega)} + \frac{\sin^2(\theta)}{n_E^2(\omega)} \right]^{-1/2} \tag{A.2}$$

The values of n_O and n_E were calculated using the Sellmeir equations for the BBO crystal [32, 33]

$$n_O^2(\lambda) = 2.7359 + 0.01878/(\lambda^2 - 0.01822) - 0.01354\lambda^2, \tag{A.3}$$
$$n_E^2(\lambda) = 2.3753 + 0.01224/(\lambda^2 - 0.01667) - 0.01516\lambda^2, \tag{A.4}$$

where λ is the wavelength at free space $\lambda = 2\pi c/\omega$ and is given in μm. With the pump wavelength $\lambda_p = 407$ nm and the wavelength of the down-converted photons $\lambda_0 = 814$ nm, we obtain $n_E(0.407) = 1.567$, $n_O(0.407) = 1.691$ and $n_O(0.814) = 1.660$. Using these values with Eq. (A.2) and solving Eq. (A.1), we calculate that the refractive index $n_{si} = n_e(\lambda = 407nm, \theta) = n_o(\lambda = 814nm)$ for pump and down-converted photons becomes

$$n_{si} = 1.66014 \tag{A.5}$$
$$\theta = 28.675°. \tag{A.6}$$

where *si* refers to signal-idler. However, θ is the angle of propagation inside the nonlinear crystal. We can use Snell law $\sin(\theta^{(i)}) = n_{si}\sin(\theta^{(t)})$ where $\theta^{(i)}$ is the angle of incidence and transmission with respect to the normal of the crystal face. The angle $\theta^{(t)}$ is given by $\theta^{(t)} = \theta - \sigma = 1.725$ where $\sigma = 30.4$ is the optics axis of the crystal. Then, the incidence angle is $\theta^{(i)} = 2.86°$.

We mount the crystal in a rotatory base in order to tilt the angle of incidence. Because of the length of the crystal (5 mm), the output of the down-converted photons is vertically shifted about 100 μm. After the interference process, the light is coupled to multimode fibers which are connected to the photodetectors. Since the circular area of the core of the multimode fiber has a diameter of 62.5 μm, the shift has to be corrected when coupling the light into the fibers by translating the position of the fiber or the focusing lenses.

A.3   Histogram of the coincidences

We use two single photon counting avalanche photodiodes (SPC-APD) working in coincidences. The efficiency is about 60 % at 814 nm wavelength. The active area is 180 μm diameter. It is very important to keep the photodetectors from receiving ambient light, because they can be destroyed (maximum counts per second is 10 millions). To avoid the background noise, we connect the APD with optical fibers. We use multimode optical fibers (NA = 0.275 and diameter of 62.5 μm). In order to couple the light into the fiber we use lens with $NA = 0.25$ and focal lens of 11 mm.

When a single photon is detected, the APD sends a TTL pulse of 2.5 V (minimum) high using a 50Ω load and 15 ns wide. The pulses are sent into the electronic coincidence detector (PicoHarp 300). We introduce a time delay between the pulses by extending one of the cable that connects to the coincidence detector. By doing that, we shift the center of the coincidence histogram and with this we can detect the four scenarios that are shown in Fig. 3.1b. Without the delay, one of the cases *iii* or *iv* in Fig. 3.1b is discarded because the detector does not measure negative delay times.

For the coincidences we use a time resolution of 4 ps, and a time window of $\tau = 3$ ns. For each step of the piezo motor, we measure the coincidences during $T = 10$ seconds in order to increase the signal to noise ratio. A typical coincidences histogram is shown in Fig. A.1a. In order to obtain the interferogram, for each histogram we integrate the coincidences between the 3 ns time window. We implement a Labview program to synchronize the piezo motor with the coincidence detector. At the same time, we measure the single counts interferogram on each photodetector in order to subtract the accidental counts, which is given by the equation $AB\tau/T$ where A and B are the single photon counts of detectors A and B (it is equivalent to the area under the coincidences peak).

We perform an interesting experiment to distinguish over the different scenarios shown in Fig. 3.1b. We increase the path-length difference to 60 cm between the interferometer arms in order to introduce a time delay of 2 ns. The histogram for this configuration is shown in Fig. A.1b. The center of the histogram is at 32 ns because we introduce about 10 m of cable to delay one of the TTL pulses generated by the photodetectors. Notice that the central peak is about twice the intensity of the side peaks because is given by the cases when both photons are reflected and when both photons are transmitted. Because they travel together, the time difference between them is 0. Then, the side peaks correspond to the cases when one photon is reflected and the other transmitted.

As we mentioned in Chapter 3, the post-selection technique introduces a path-length difference large enough to separate the four scenarios and then selects the central peak. By doing this, the coincidences interferogram is given by the superposition of both photons being reflected plus both photons being transmitted. Therefore, the coincidences interferogram is equal to a single photon interferogram with fringes oscillating at twice its central frequency, similar to Fig. 3.4a but with maximum visibility of 1.

A.4 Alignment and balancing of the optical paths

There are two principal requirements for the construction of the two-photon Michelson interferometer: alignment and length balancing of the two optical paths. Alignment is difficult because the beam cannot be viewed without an expensive low-intensity light detector array and since the acquisition time is slow (10 seconds), it is not possible to scan the reference arm to find the equal path-length position.

Alignment is achieved by introducing a 633 nm helium-neon laser in the optical pathway of the down-converted photons. The optical pathway is guided using apertures. The location of the apertures is optimized by maximizing the single counts. After optimizing the apertures with the He-Ne laser, we proceed to generate the down-converted photons using the nonlinear crystal. Since the polarization of the pump laser is vertical, the plane of the optics axis should
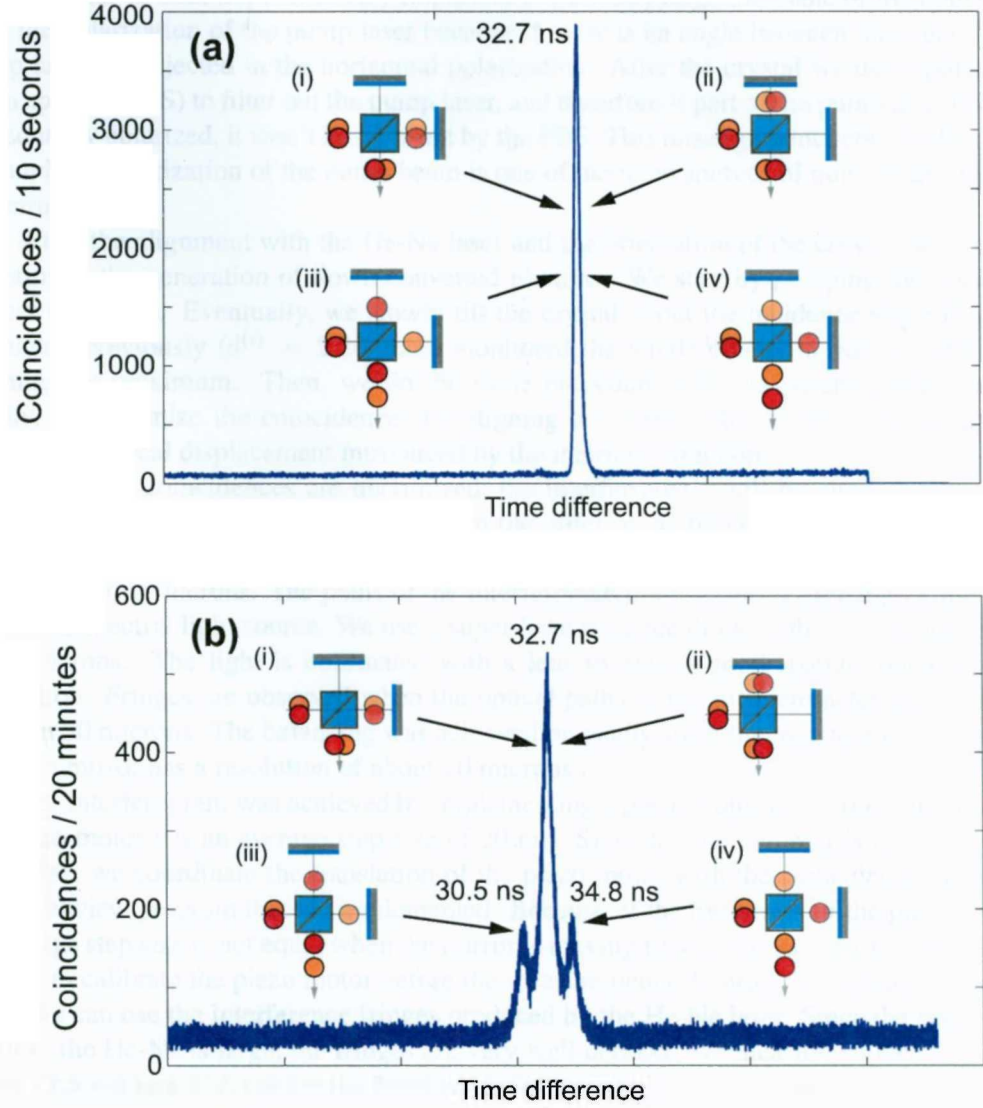
Figure A.1: (a) Histogram of coincidences for down-converted photons. The histogram shows the number of coincidences as a function of the time delay between the two photons. The coincidences peak indicates that the photons are emitted simultaneously. The position of the peak is shifted at 32.7 ns by introducing about 10 meters of delay in the coincidence circuit. (b) Histogram of the coincidences when the path-length difference of the interferometer arms is about 60 cm, which introduces a time delay between signal and idler photons of about 2 ns when they travel different optical pathways.

be in the vertical position as well. To confirm the orientation of the optics axis of the crystal, we can visualize a thin line through the crystal and rotate the crystal until we observe two lines. When the separation between the two lines is maximum, the plane of the optics axis is

perpendicular to both lines. It is very important to perfectly align the plane of the optics axis with the polarization of the pump laser because if there is an angle between then, part of the pump laser is projected in the horizontal polarization. After the crystal we use a polarizing beam splitter (PBS) to filter out the pump laser, and therefore if part of the pump laser become horizontally polarized, it won't be filter out by the PBS. This misalignment between the optics axis and the polarization of the pump beam is one of the main sources of noise in this kind of experiment.

After the alignment with the He-Ne laser and the orientation of the crystal, we proceed to optimize the generation of down-converted photons. We start by pumping the crystal at normal incidence. Eventually, we slowly tilt the crystal about the incidence angle that was calculated previously ($\theta^{(i)} = 2.86°$) and monitored the single counts in one detector until reaching the maximum. Then, we do the same procedure with the second photodetector. Finally, we optimize the coincidences by aligning the fibers. Remember that we have to correct the vertical displacement introduced by the internal refraction.

When the coincidences are maximized, the interferometer will be aligned. But since the coherence length of the He-Ne laser is in the order of centimeters, the optical paths are unlikely to be balanced. Remember that the coherence length of the down-converted photons is in the order of microns. The paths of the interferometer are balanced exchanging the laser by a broad spectral light source. We use a super-luminescence diode with a coherence length of 50 microns. The light is collimated with a lens to ensure good spatial coherence and collimation. Fringes are observed when the optical paths of the interferometer are balanced to within 50 microns. The balancing was achieved manually since the translation stage of the reference mirror has a resolution of about 10 microns.

The interferogram was achieved by implementing a piezo motor to the reference mirror. The piezo motor has an average step size of 20 nm. Since the piezo motor is activated by a TTL pulse, we coordinate the translation of the piezo motor with the coincidence detection with a Labview program that we implemented. Because of the hysteresis of the piezo motor, the average step size is not equal when the mirror is moving forward or backwards. Therefore, we have to calibrate the piezo motor before the measurements. In order to calibrate the piezo motor, we can use the interference fringes produced by the He-Ne laser. Since the coherence length of the He-Ne is large, the fringes are very well defined. We measured an average step size of 17.5 nm and 22.6 nm for the forward and backward direction respectively.

A.5 Experimental implementation

The complete experimental arrangement is shown in Fig. A.2. Description of each component can be found in Table A.1 and pictures of the experiment are shown in Figures A.3, A.4 and A.5.
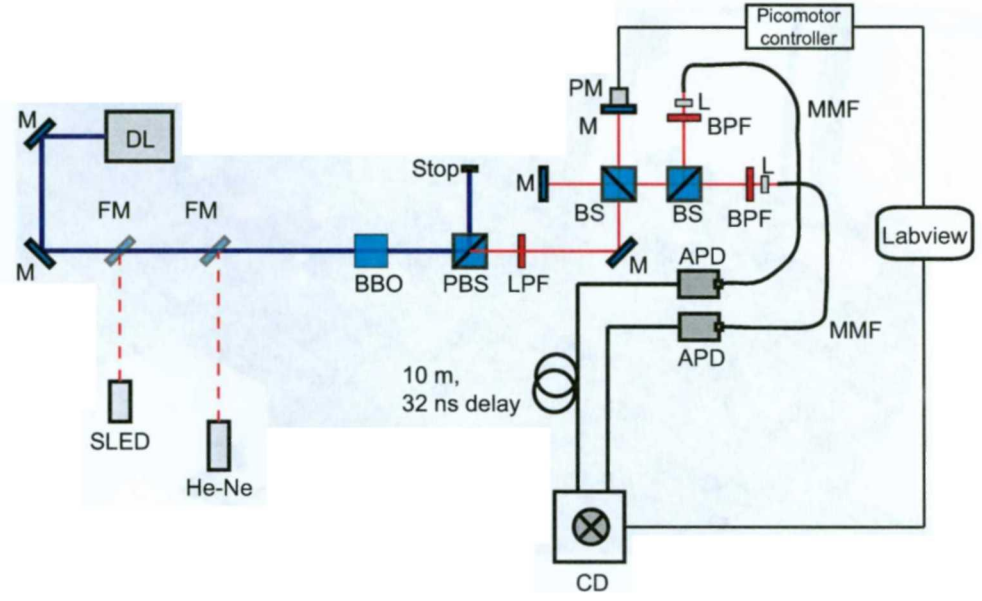
Figure A.2: Experimental arrangement. Refer to table A.1 for the details of the components.

Table A.1: Experimental components

| Tag	Component	Comments	Price (USD)
M	Mirror	Thorlabs $R > 96\%$	$50.00
FM	Flipper mirror (2)	Newport	$ 440.00
BBO	β-barium borate crystal	United Crystals 5 mm^3	$1,000.00
PBS	Polarizing beam splitter cube	Thorlabs PBS251	$203.00
BS	50:50 Beam splitter cube (2)	Thorlabs CM1-BS014	$560.00
LPF	Long-pass filter	Chroma HQ700LP	$275.00
BPF	Band-pass filter (2)	Chroma D810/10X	$400.00
MMF	Multi-mode fiber (2)	Thorlabs, $NA = 0.275$	$30.00
L	Lens (2)	Thorlabs C220TME-B	$160.00
APD	Avalanche Photodiode (2)	Perkin Elmer	$8,000.00
PM	Picomotor	New Focus	$600.00
CD	Coincidence detector	Picoharp 300	$10,000.00
DL	Diode Laser	Coherent CUBE 407 nm	$7,000.00
He-Ne	He-Ne laser	Thorlabs	$1,000.00
SLED	Superluminescence diode	Thorlabs	$2,800.00
			~$33,000.00
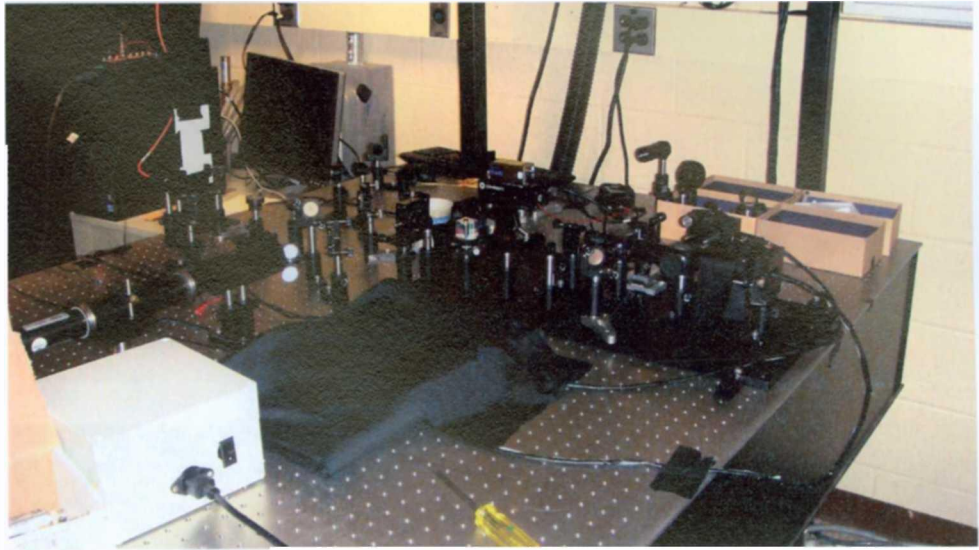
Figure A.3: Experimental setup.
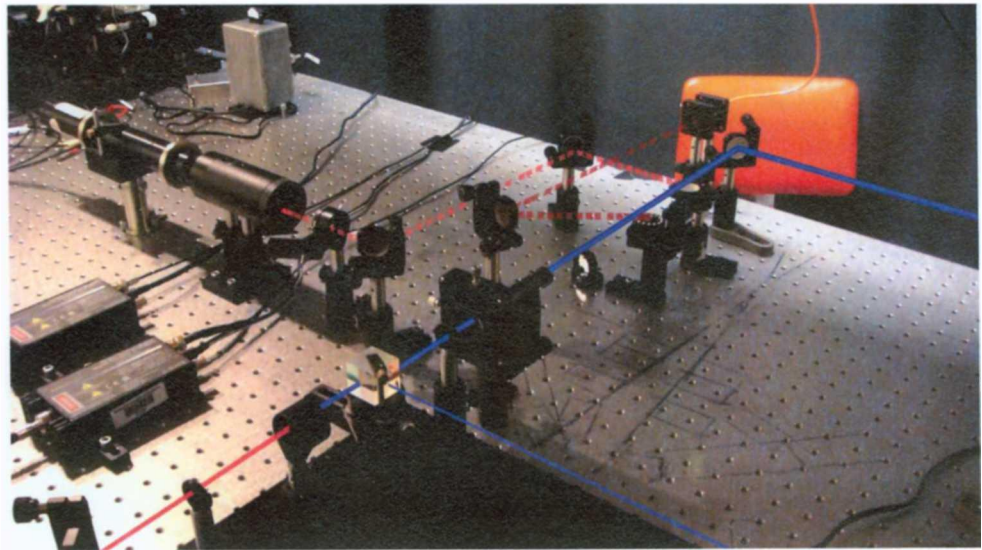
Figure A.4: Alignment procedure. The He-Ne laser is used for the alignment of the two-photon Michelson interferometer. For balancing the interferometer arms, a SLED with a coherence length of about 50 μm is implemented.
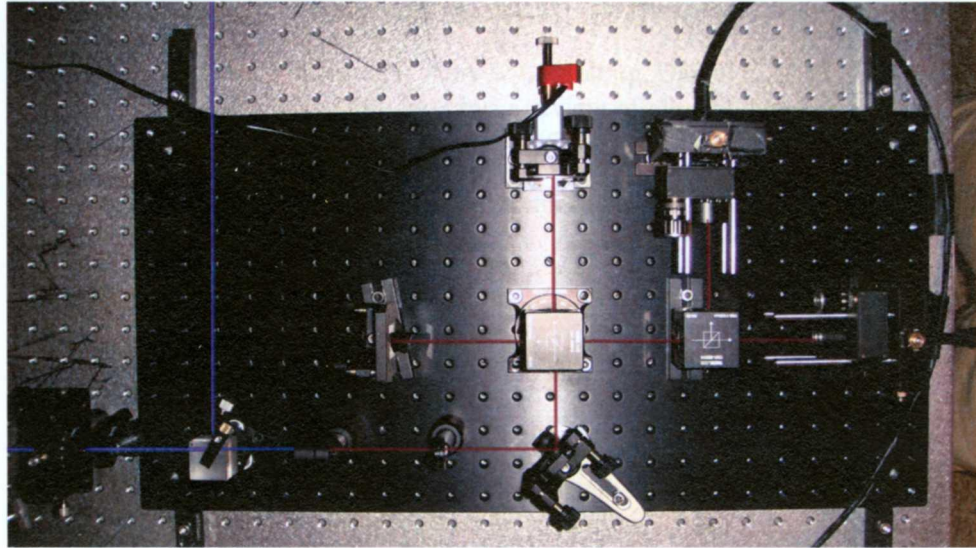
Figure A.5: Two-photon Michelson interferometer.

Bibliography

[1] J.M. Schmitt. Optical coherence tomography (OCT): a review. *Selected Topics in Quantum Electronics, IEEE Journal of*, 5(4):1205 –1215, jul/aug 1999.

[2] D Huang, EA Swanson, CP Lin, JS Schuman, WG Stinson, W Chang, MR Hee, T Flotte, K Gregory, CA Puliafito, and al. et. Optical coherence tomography. *Science*, 254(5035):1178–1181, 1991.

[3] Adam M. Zysk, Freddy T. Nguyen, Amy L. Oldenburg, Daniel L. Marks, and Stephen A. Boppart. Optical coherence tomography: a review of clinical development from bench to bedside. *Journal of Biomedical Optics*, 12(5):051403, 2007.

[4] Wojciech J. Walecki and Phuc Van. US Patent 7,116,429 B1, Determining thickness of slabs of materials, 2003.

[5] John Hart. Lumetrics, 2012. http://www.lumetrics.com/.

[6] Ayman F. Abouraddy, Magued B. Nasr, Bahaa E. A. Saleh, Alexander V. Sergienko, and Malvin C. Teich. Quantum-optical coherence tomography with dispersion cancellation. *Phys. Rev. A*, 65:053817, May 2002.

[7] Magued B. Nasr, Bahaa E. A. Saleh, Alexander V. Sergienko, and Malvin C. Teich. Demonstration of Dispersion-Canceled Quantum-Optical Coherence Tomography. *Phys. Rev. Lett.*, 91:083601, Aug 2003.

[8] Malvin Teich, Bahaa Saleh, Franco Wong, and Jeffrey Shapiro. Variations on the theme of quantum optical coherence tomography: a review. *Quantum Information Processing*, 10:1–21, 2011.

[9] C. K. Hong, Z. Y. Ou, and L. Mandel. Measurement of subpicosecond time intervals between two photons by interference. *Phys. Rev. Lett.*, 59:2044–2046, Nov 1987.

[10] S. Tanzilli, A. Martin, F. Kaiser, M.P. De Micheli, O. Alibart, and D.B. Ostrowsky. On the genesis and evolution of Integrated Quantum Optics. *Laser and Photonics Reviews*, 6(1):115–143, 2012.

[11] Hector Cruz-Ramirez, Roberto Ramirez-Alarcon, Maria Corona, Karina Garay-Palmet, and Alfred B. U'Ren. Spontaneous Parametric Processes in Modern Optics. *OPN*, 22, November 2011.

55

[12] O. Thomas, Z. L. Yuan, and A. J. Shields. Practical photon number detection with electric field-modulated silicon avalanche photodiodes. *Nat. Commun.*, 3, January 2012.

[13] Leonard Mandel and Emil Wolf. *Optical Coherence and Quantum Optics*. Cambridge University Press, 1995.

[14] Max Born and Emil Wolf. *Principles of Optics*. Cambridge University Press, 7 edition, 1999.

[15] Robert W. Boyd. *Nonlinear Optics*. Elsevier, 2008.

[16] Z. Y. Jeff Ou. *Multi-Photon Quantum Interference*. Springer, 2007.

[17] A. Einstein, B. Podolsky, and N. Rosen. Can Quantum-Mechanical Description of Physical Reality Be Considered Complete? *Phys. Rev.*, 47:777–780, May 1935.

[18] J. S. Bell. On the Einstein-Podolsky-Rosen Paradox. *Physics*, 1:195–200, 1964.

[19] Stuart J. Freedman and John F. Clauser. Experimental Test of Local Hidden-Variable Theories. *Phys. Rev. Lett.*, 28:938–941, Apr 1972.

[20] Alain Aspect, Philippe Grangier, and Gérard Roger. Experimental Tests of Realistic Local Theories via Bell's Theorem. *Phys. Rev. Lett.*, 47:460–463, Aug 1981.

[21] Edward S. Fry and Randall C. Thompson. Experimental Test of Local Hidden-Variable Theories. *Phys. Rev. Lett.*, 37:465–468, Aug 1976.

[22] Asher Peres. Separability Criterion for Density Matrices. *Phys. Rev. Lett.*, 77:1413–1415, Aug 1996.

[23] Michal Horodecki, Pawel Horodecki, and Ryszard Horodecki. Separability of mixed states: necessary and sufficient conditions. *Physics Letters A*, 223:1–8, November 1996.

[24] Artur Ekert and Peter L. Knight. Entangled quantum systems and the Schmidt decomposition. *American Journal of Physics*, 63(5):415–423, 1995.

[25] Lu-Ming Duan, G. Giedke, J. I. Cirac, and P. Zoller. Inseparability Criterion for Continuous Variable Systems. *Phys. Rev. Lett.*, 84:2722–2725, Mar 2000.

[26] Julio T. Barreiro, Nathan K. Langford, Nicholas A. Peters, and Paul G. Kwiat. Generation of Hyperentangled Photon Pairs. *Phys. Rev. Lett.*, 95:260501, Dec 2005.

[27] Michael A. Horne, Abner Shimony, and Anton Zeilinger. Two-particle interferometry. *Phys. Rev. Lett.*, 62:2209–2212, May 1989.

[28] D. A. Kleinman. Theory of Optical Parametric Noise. *Phys. Rev.*, 174:1027–1041, Oct 1968.

[29] B. Ya. Zel'dovich and D. N. Klyshko. Field statistics and parametric luminescence. *JETP lett.*, 9(1):40–43, 1969.

[30] David C. Burnham and Donald L. Weinberg. Observation of Simultaneity in Parametric Production of Optical Photon Pairs. *Phys. Rev. Lett.*, 25:84–87, Jul 1970.

[31] Yuan Zhen-Sheng, Bao Xiao-Hui, Lu Chao-Yang, Zhang Jun, Peng Cheng-Zhi, and Pan Jian-Wei. Entangled Photons and Quantum Communications. *Physics Reports*, 497:1–40, 2010.

[32] V. G. Dimitriev, G. G. Gurzadyan, and D. N. Nikogosyan. *Handbook of Nonlinear Optical Crystals*. Springer, 3 edition, 1999.

[33] D. Eimerl, L. Davis, S. Velsko, E. K. Graham, and A. Zalkin. Optical, mechanical, and thermal properties of barium borate. *Journal of Applied Physics*, 62(5):1968–1983, 1987.

[34] United Crystals Company. United crystals, 2011. http://www.unitedcrystals.com.

[35] R. P. Feynman, R. B. Leighton, and M. Sands. *The Feynman Lectures on Physics*. Addison-Wesley, 2 edition, 1964.

[36] L. Mandel. Quantum effects in one-photon and two-photon interference. *Rev. Mod. Phys.*, 71:S274–S282, Mar 1999.

[37] N. Boeuf, D. Branning, I. Chaperot, E. Dauler, S. Guérin, G. Jaeger, A. Muller, and A. Migdall. Calculating characteristics of noncollinear phase matching in uniaxial and biaxial crystals. *Optical Engineering*, 39(4):1016–1024, 2000.

[38] J. D. Franson. Bell inequality for position and time. *Phys. Rev. Lett.*, 62:2205–2208, May 1989.

[39] J. Brendel, E. Mohler, and W. Martienssen. Time-resolved dual-beam two-photon interferences with high visibility. *Phys. Rev. Lett.*, 66:1142–1145, Mar 1991.